THE ASTROPHYSICAL JOURNAL SUPPLEMENT SERIES, 106:621–646, 1996 October

COMPREHENSIVE MULTIWAVELENGTH OBSERVATIONS OF THE 1992 JANUARY 7 SOLAR FLARE

ADRIANA V. R. SILVA,[1] STEPHEN M. WHITE,[2] ROBERT P. LIN,[3,4] IMKE DE PATER,[1] DALE E. GARY,[5]
JAMES M. MCTIERNAN,[3] HUGH S. HUDSON,[6] J. GERRY DOYLE,[7]
MONA J. HAGYARD,[8] AND MUKUL R. KUNDU[2]
Received 1996 February 12; accepted 1996 April 17

ABSTRACT

Observations of a solar flare that occurred at 2022 UT on 1992 January 7, during the 1991 December/1992 January Max '91 campaign, are presented. This flare was observed simultaneously in Hα, radio (at microwave and millimeter wavelengths), and soft and hard X-rays (by the *Yohkoh* spacecraft) with high spatial and moderate spectral resolution. A comparison of magnetograms before and after the flare shows evidence of the emergence of new magnetic flux of opposite polarity at the flare site. Although this flare was only of moderate size (*GOES* classification C8.9 and Hα importance SF), it exhibited several distinct bursts and at least 10 spatially distinct hard/soft X-ray sources. Cospatial Hα brightenings suggest that most of the X-ray sources are located at footpoints of magnetic loops. Two of the hard X-ray sources have no Hα counterparts and are therefore believed to be located at loop tops. The flare consisted of three bursts of particle acceleration followed by a purely thermal phase. High spectral resolution Ca XIX line profiles indicate upflows shortly after the second acceleration phase. Analysis of the microwave/hard X-ray/soft X-ray emission from individual sources provides information on the radio emission mechanisms, the energetic electron population, the magnetic field strength, and the plasma density. These parameters were estimated for the two microwave sources observed during the third acceleration burst; these sources were simultaneously detected in soft X-rays, and one of the sources is also seen in hard X-ray maps. Although the microwave emission is consistent with the gyrosynchrotron mechanism, the millimeter emission, which peaks during the thermal phase when all nonthermal activity has ceased, is likely due to thermal bremsstrahlung from the soft X-ray–emitting hot plasma. The energy lost to collisions by the energetic (>15 keV) electrons and the energy contained in the thermal plasma are calculated for each source. The energy injected by the nonthermal electrons from all sources is estimated to be $\sim 10^{30}$ ergs. Only the soft X-ray sources with gradual time profiles seem to show the Neupert effect.

Subject headings: Sun: flares — Sun: magnetic fields — Sun: radio radiation — Sun: X-rays, gamma rays

1. INTRODUCTION

Solar flares emit radiation over the entire electromagnetic spectrum, from gamma rays to kilometer-wavelength radio waves. In order to understand the physical processes involved and obtain a complete picture of a solar flare, multiwavelength coverage with good spectral and spatial resolution is required. The Max '91 solar observing campaigns were designed to provide comprehensive, simultaneous ground-based and satellite-borne observations.

Simultaneous multiwavelength observations of a flare can provide information about the energetic particles, the plasma, and the magnetic field. For example, hard and soft X-rays have been compared to Hα emission by Nitta, Dennis, & Kiplinger (1990), Kiplinger, Labow, & Orwig (1991), and Neidig et al. (1993). Simultaneous flare emissions in X-rays, Hα, and microwaves have been analyzed by several authors (Holman, Kundu, & Kane 1989; Gary & Hurford 1990; Bastian & Gary 1992; Kundu, White, & Welch 1991; White et al. 1992). Ultraviolet imaging has been used as a proxy method for locating the hard X-ray sources (Schwartz & Drake 1991). Multiwavelength observations of bursts at millimeter and microwave frequencies were analyzed by White et al. (1992) and Lim et al. (1992). Based on the similarity between time profiles, special attention has been paid to the comparison of microwaves and hard X-rays (Kundu 1961; Willson et al. 1990; Aschwanden, Dennis, & Benz 1991; Crannell et al. 1991). It is important, however, to establish the spatial relationship of the microwave and hard X-ray sources; this requires high spatial resolution in both wavelength regimes (Kundu, White, & Schmahl 1989; Nitta et al. 1991). Spectral information is crucial to determining the mechanism of the X-ray and radio emissions.

In this paper, comprehensive spatially and spectrally resolved multiwavelength observations are presented for a flare that occurred on 1992 January 7 at ~2022 UT, in the large target-region complex AR 6993/6994, during the Max '91 campaign in 1991 December/1992 January. The flare was located at S16 W18, in AR 6994, and its Hα importance was SF. *GOES* reports that the soft X-ray burst reached a level of C8.9 (soft X-ray energy flux of 8.9×10^{-3} ergs cm^{-2}

[1] Department of Astronomy, University of California, Berkeley, Berkeley, CA 94720.
[2] Department of Astronomy, University of Maryland, College Park, MD 20742.
[3] Space Sciences Laboratory, University of California, Berkeley, Berkeley, CA 94720.
[4] Also Department of Physics, University of California, Berkeley.
[5] California Institute of Technology, Solar Astronomy, 264-33, Pasadena, CA 91103.
[6] Institute for Astronomy, 2680 Woodlawn Drive, University of Hawaii, Honolulu, HI 96822.
[7] Armagh Observatory, College Hill, Armagh BT61 9DG, Northern Ireland.
[8] Marshall Space Flight Center, Huntsville, AL 35812.

TABLE 1

INSTRUMENTS THAT OBSERVED THE 1992 JANUARY 7 FLARE

Instrument	Wavelength	Pointing Coordinates[a]	Field of View
MSFC (Hα)......	6563 Å	312, 183	360″
GOES	0.5–4 and 1–8 Å	0, 0	Full disk
Yohkoh:			
SXT	3–60 Å	312, −183	640″, 320″, 160″
HXT...........	15–100 keV	312, −183	126″
BCS	1.7–5.1 Å	0, 0	Full disk
VLA:			
2022 UT	5.0 GHz	300, −200	600″
2025 UT	0.33 and 1.5 GHz	143, −245	Full disk
RSTN	0.245–8.8 GHz	0, 0	Full disk
OVRO	1–18 GHz	290, −97	$46\farcs5/\nu_{GHz}$
BIMA	89 GHz	190, −190	120″

[a] In arcseconds west and north from disk center, respectively.

s^{-1}), a moderate flare in intensity. A vector magnetogram was obtained by the Marshall Space Flight Center prior to the flare, and a normal longitudinal magnetogram was taken a day after the flare at Kitt Peak National Observatory.

The Soft X-ray Telescope (SXT) on the *Yohkoh* satellite provided soft X-ray (3–60 Å) images with high spatial resolution ($2\farcs5$), and hard X-ray maps (14–53 keV) at $\sim 5''$ resolution were produced by the *Yohkoh* Hard X-ray Telescope (HXT). *Yohkoh*'s Bragg Crystal Spectrometer (BCS) provided high spectral resolution measurements of line shapes for the Ca XIX, Fe XXV, and S XV lines.

The Very Large Array (VLA, operated by NRAO[9]) imaged the flare at 1.5 and 5 GHz with high spatial resolution ($3\farcs9$ at 5 GHz and $7\farcs0$ at 1.5 GHz) while the solar-dedicated frequency-agile interferometer at the Owens Valley Radio Observatory (OVRO) provided maps of the sources from 1 to 18 GHz with high spectral resolution (better than 0.5 GHz). The Radio Solar Telescope Network (RSTN) observations offer microwave total-power spectra with high temporal resolution (1 s). This flare was simultaneously observed by the Berkeley-Illinois-Maryland Array (BIMA) at 3.3 mm (89 GHz).

[9] The National Radio Astronomy Observatory is a facility of the National Science Foundation operated under cooperative agreement by Associated Universities, Inc.

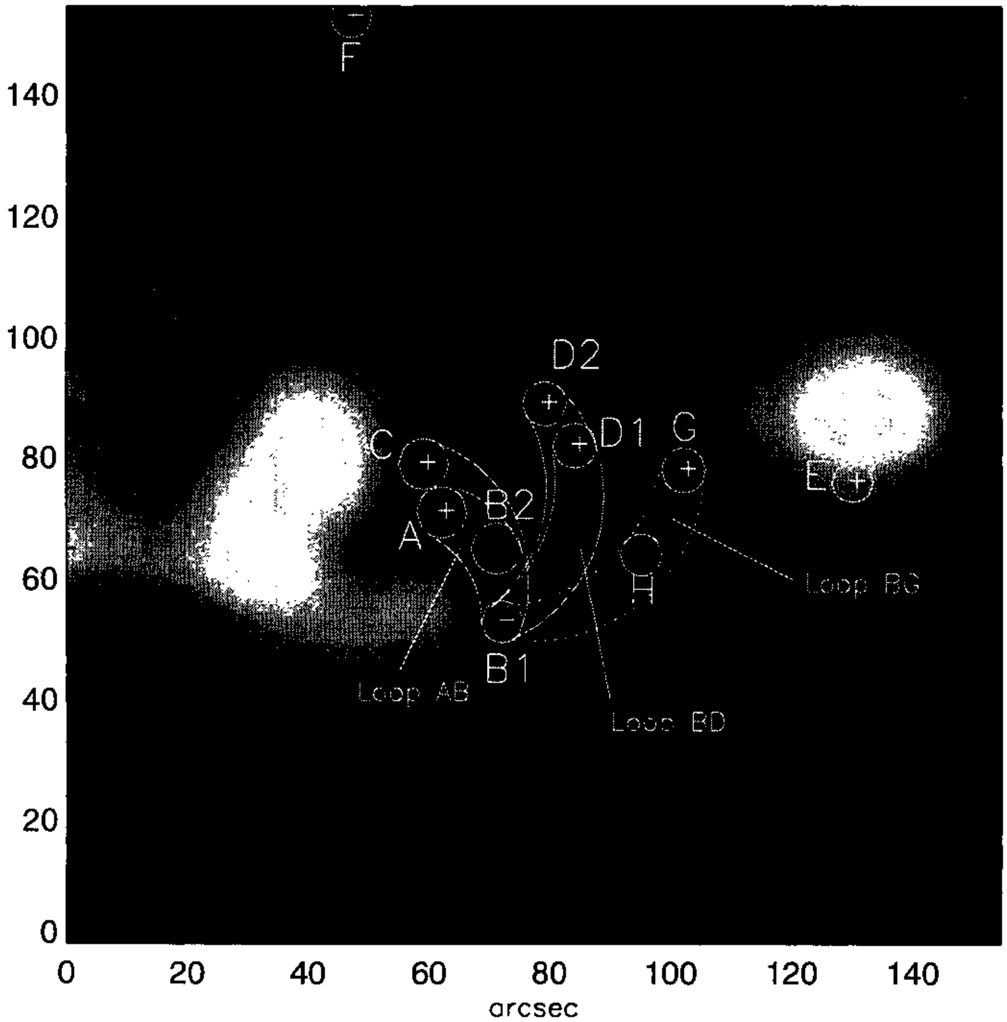

FIG. 1.—Sketch of the main magnetic loops. Loop AB connects source A to B1, and loop BD joins sources B1 and D1/D2. The dotted lines represent a possible magnetic loop connecting source G to B1. The underlying photospheric magnetogram from MSFC is plotted as a gray scale.

TABLE 2

SOURCES OF THE 1992 JANUARY 7 FLARE

SOURCE/ INSTRUMENT[a]	PHASE DETECTED				LOCATION[b]	UNDERLYING MAGNETIC FIELD POLARITY
	P1	PH	P2	PM		
A (63″, 70″):						
SXT		✓	✓	✓	F	+
MSFC Hα	✓	✓	✓			
OVRO			✓			
VLA 5.0	✓					
B1 (72″, 53″):						
SXT	✓	✓	✓	✓	F	−
HXT LO	✓	✓				
HXT M1	✓					
MSFC Hα	✓		✓			
B2 (71″, 61″):						
SXT		✓	✓	✓	T	...
HXT LO		✓	✓			
HXT M1			✓			
OVRO			✓			
C (56″, 81″):						
SXT	✓	✓			F	+
HXT LO	✓		✓			
HXT M1	✓		✓			
MSFC Hα	✓	✓	✓			
D1 (84″, 82″):						
SXT	✓	✓			F	+
HXT LO	✓					
HXT M1	✓					
MSFC Hα	✓	✓				
D2 (79″, 89″):						
SXT		✓	✓		F	+
HXT LO		✓	✓			
HXT M1			✓			
MSFC Hα	✓	✓	✓			
E (118″, 76″):						
SXT	✓				F	+
HXT M1	✓					
MSFC Hα	✓	✓				
F (50″, 150″):						
SXT	✓				F	−
MSFC Hα	✓	✓	✓			
OVRO	✓					
VLA 5.0	✓					
VLA 1.5				✓		
G (102″, 78″):						
SXT	✓				F	+
HXT LO	✓					
HXT M1	✓					
MSFC Hα	✓	✓				
H (95″, 64″):						
HXT LO		✓			T	...
HXT M1			✓			
VLA 5.0	✓					
J (east):						
VLA 1.5			✓	✓	T?	...

[a] Coordinates are the source's position with respect to SXT full-resolution images (e.g., Fig. 1).

[b] F = footpoint and T = loop-top source.

Table 1 contains the energy range, pointing coordinates in arcseconds from disk center, and field of view of each instrument. Details of the instruments and their observing modes are given in Appendix A. To help guide the reader through the complex morphology of the flare, the next section presents a brief summary of the chain of events. A description of the magnetic configuration is given in § 3. The flare's temporal evolution is discussed in § 4, and § 5 describes the Hα emission. Section 6 presents the soft X-ray data and hard X-ray maps and spectra. The microwave and millimeter observations are discussed in § 7. The flare energetics and a detailed comparison and analysis of the millimeter, microwave, and X-ray emission follow in § 8. Finally, § 9 summarizes the conclusions.

2. OVERVIEW

The flare occurred in a complex of two interacting active regions, at a site of emerging new magnetic flux. The most intense soft X-ray emission and most of the hard X-ray emission occurred in two compact magnetic loops, AB and BD (see Fig. 1). Early in the flare, a third loop, BG, is important. Four distinct phases, denoted in time order as P1, PH, P2, and PM, can be distinguished in the flare's temporal evolution. The first and third phases (P1 and P2) are characterized by strong electron acceleration to well above 25 keV. Electron acceleration probably occurs in the second phase (PH), but the X-ray spectrum falls steeply, with little or no emission detected above 25 keV. The last phase (PM) appears to be purely thermal.

Each phase involves multiple sources (labeled in Fig. 1), and the individual sources change from one phase to another. Table 2 presents the sources seen by the different instruments during each phase. Common to all phases are soft X-ray, hard X-ray, and radio emission at location B2, near or above the top of loop AB. Source B2 is seen in the temperature maps from SXT at all times as the hottest thermal source in the region.

Besides the X-ray and radio sources located in or near loops AB, BD, and BG, there are several distant ($\geq 100''$, or 7×10^4 km, away) sources that brighten during the flare. These are seen primarily in microwave and soft X-ray emission because of the larger field of view at these wavelengths. In addition, during the interval from PH to P2, blueshifts are detected in the Ca XIX line emission, indicating upflows. Finally, the millimeter-wave emission is observed to peak at PM, when nonthermal activity has ceased.

3. MAGNETIC CONFIGURATION

The Marshall Space Flight Center (MSFC) obtained a vector magnetogram 20 minutes before the flare (Fig. 2, *top*), and the Kitt Peak National Observatory (KPNO) provided a standard longitudinal magnetogram taken approximately a day later (Fig. 2, *bottom*). The two active regions are aligned in the east-west direction, both with positive-polarity (*white*) leading spots. The northern region, AR 6993, is basically composed of two spots separated by 180″. The southern region, AR 6994, is more complex, with several spots of mixed polarity in its central region.

NOAA Boulder classified AR 6993/6994 for this day magnetically as "beta-delta" (a pair of dominant spots of opposite polarity, where some spots have umbrae of opposite polarities in a single penumbra). This complex region actually has two magnetic delta spots, one in each active region, and each was a site of flare activity. Not surprisingly, the main soft X-ray source occurred above the southernmost of these spots (indicated by arrows in Fig. 2), located in AR 6994 at (+310″, −190″) with respect to disk center. This is precisely the position of the reported optical SF flare.

The top panel of Figure 2 shows the azimuthal magnetic field overlaid on the longitudinal magnetic field intensities (*gray scale*). A sheared magnetic field is evident along the neutral line of one of the delta spots (*arrow*), close to where the flare occurred. The magnitude of the magnetic field in the vicinity of the flare brightenings ranges from 500 to

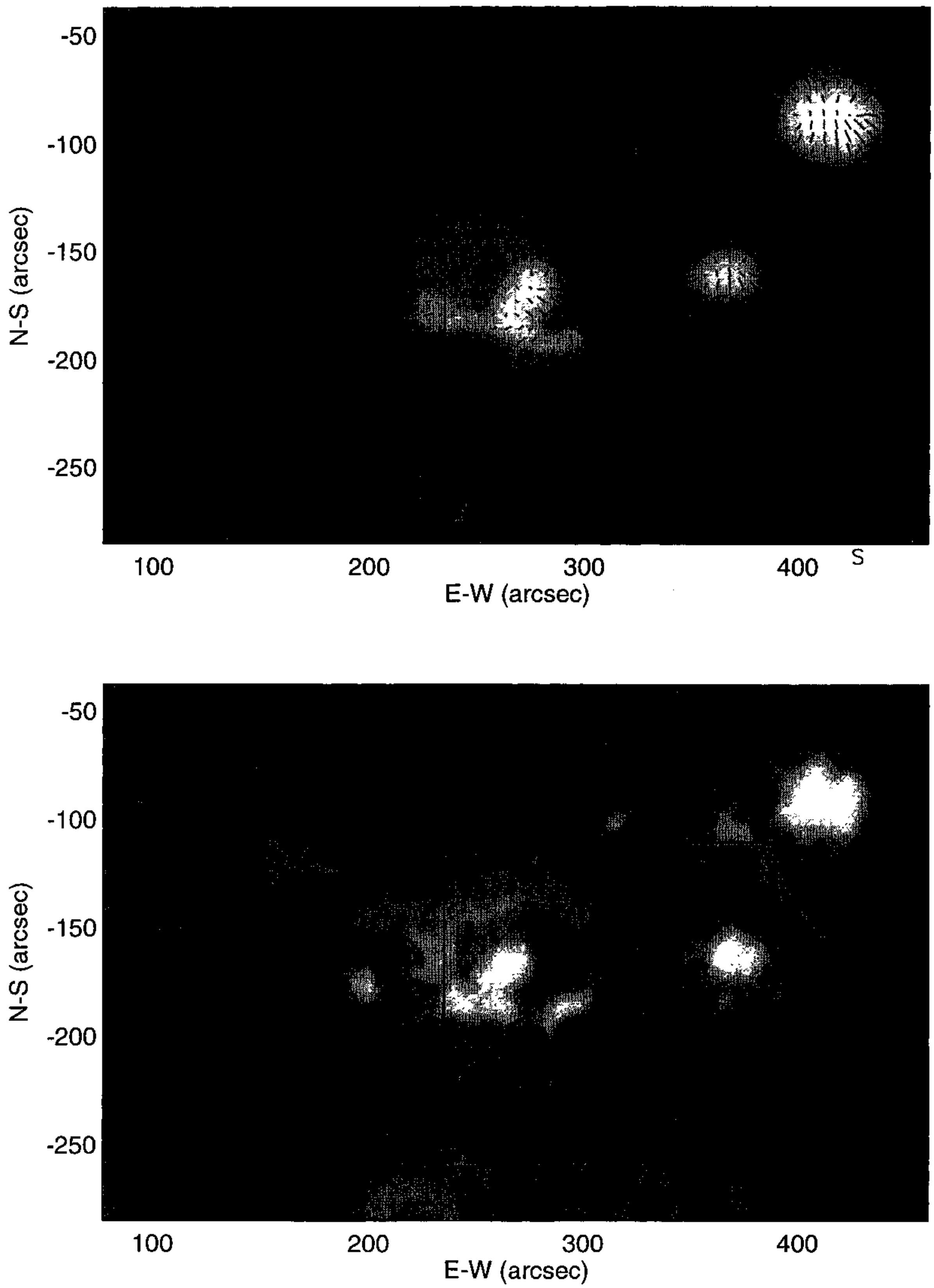

FIG. 2.—*Top*: MSFC vector magnetogram, with the azimuthal magnetic field overplotted on the longitudinal magnetic field (*gray scale*). Note the sheared magnetic field along the neutral line (*arrow*). *Bottom*: KPNO magnetogram of the same region. This magnetogram was taken on 1992 January 8 and rotated back to the time of the flare. The box shows the field of view of the *Yohkoh* SXT full-resolution images.

1000 G. A comparison of the preflare MSFC magnetogram and the postflare KPNO magnetogram seems to indicate the emergence of new negative polarity in the delta spot of AR 6993, close to where the flare occurred (*left of arrow*). The boxes in Figure 2 represent *Yohkoh*'s SXT field of view during flare mode.

The SXT soft X-ray image taken 20 minutes prior to the flare's onset (Fig. 3) shows an intricate array of loops, which connects the two active regions. In this figure, the X-ray data are shown in gray scale while the contours are from the SXT white-light image and show the locations of sunspots. The bright feature at the center of Figure 3, which corresponds to source D1 (see Fig. 1), shows evidence of preflare heating even at this stage. Superposed on the figure are the BIMA and OVRO (10 GHz) fields of view and the *Yohkoh* SXT field of view (*square*) for the full-resolution flare images.

4. TEMPORAL EVOLUTION

Figure 4 shows the time profiles of the 1992 January 7 flare as seen by the different instruments. The hard and soft X-ray time profiles are shown in Figure 4*a*. The HXT data, which begin at 2021:50 UT, as *Yohkoh* came out of Earth's shadow, show two main bursts in the medium-energy M1 (23–33 keV) channel, namely, P1 at ~2022:22 UT and P2 at ~2024:56 UT. The time profile of the HXT low-energy (LO, 14–23 keV) X-rays shows an intermediate peak at 2023:30 UT (PH). The soft X-ray emission observed by *GOES* (1–12 Å) and SXT rises monotonically and peaks later in the flare, at ~2026 UT (PM). The *GOES* high-energy channel (0.5–4 Å) peaks just after P2. This is followed by a slow decay lasting over 1 hr.

The microwave-emission time profiles measured by the VLA, OVRO, and RSTN (total power) are shown in Figure

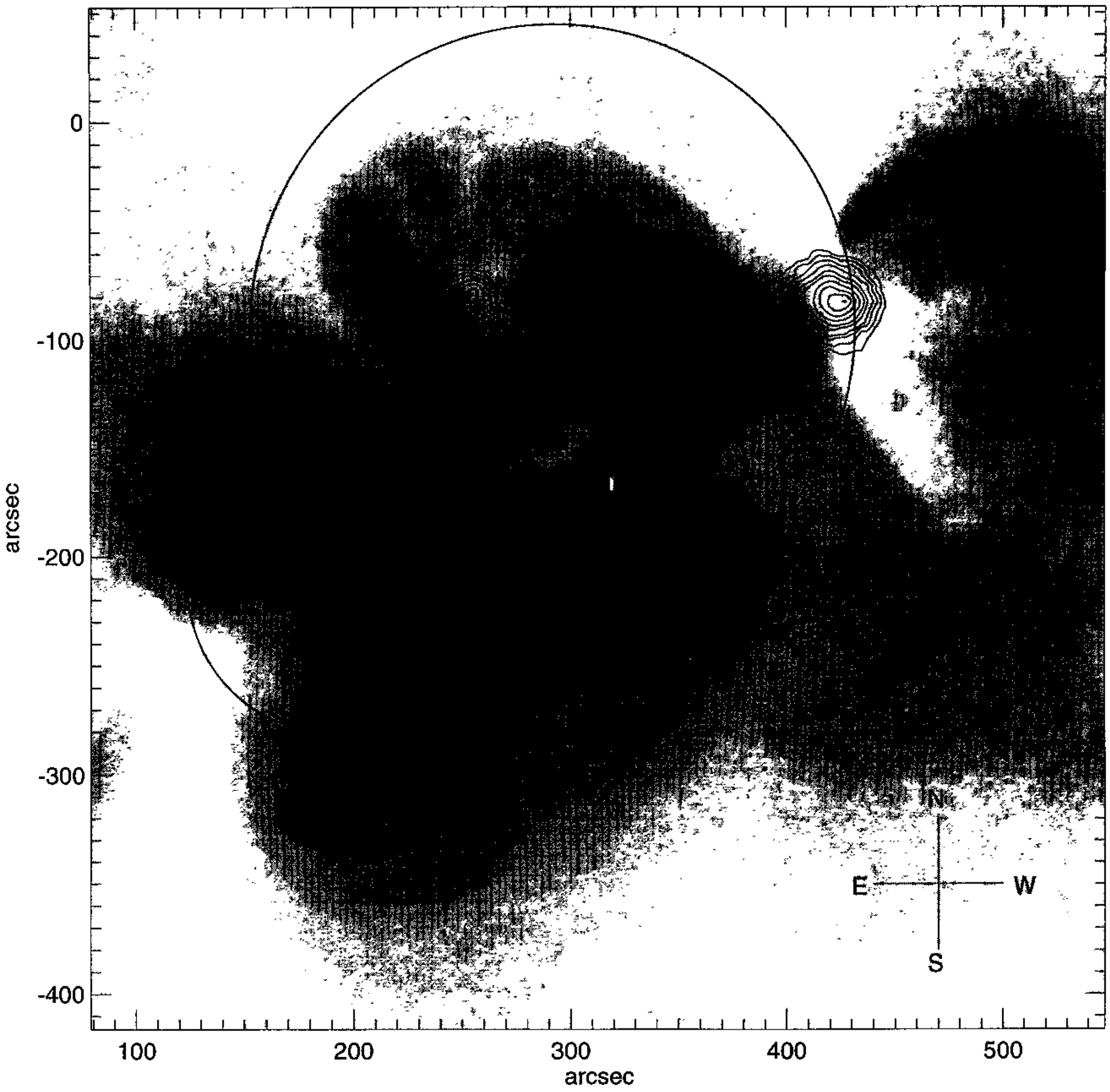

FIG. 3.—*Yohkoh* SXT preflare image taken at 1954 UT, with overlaid contours of white-light emission showing the sunspots as seen through the same soft X-ray telescope. The soft X-ray emission outlines the magnetic loops and their topology in the corona over the region. The circles correspond to BIMA and OVRO (10 GHz) fields of view. Also superposed is the square field of view of the full-resolution SXT images (see Fig. 6).

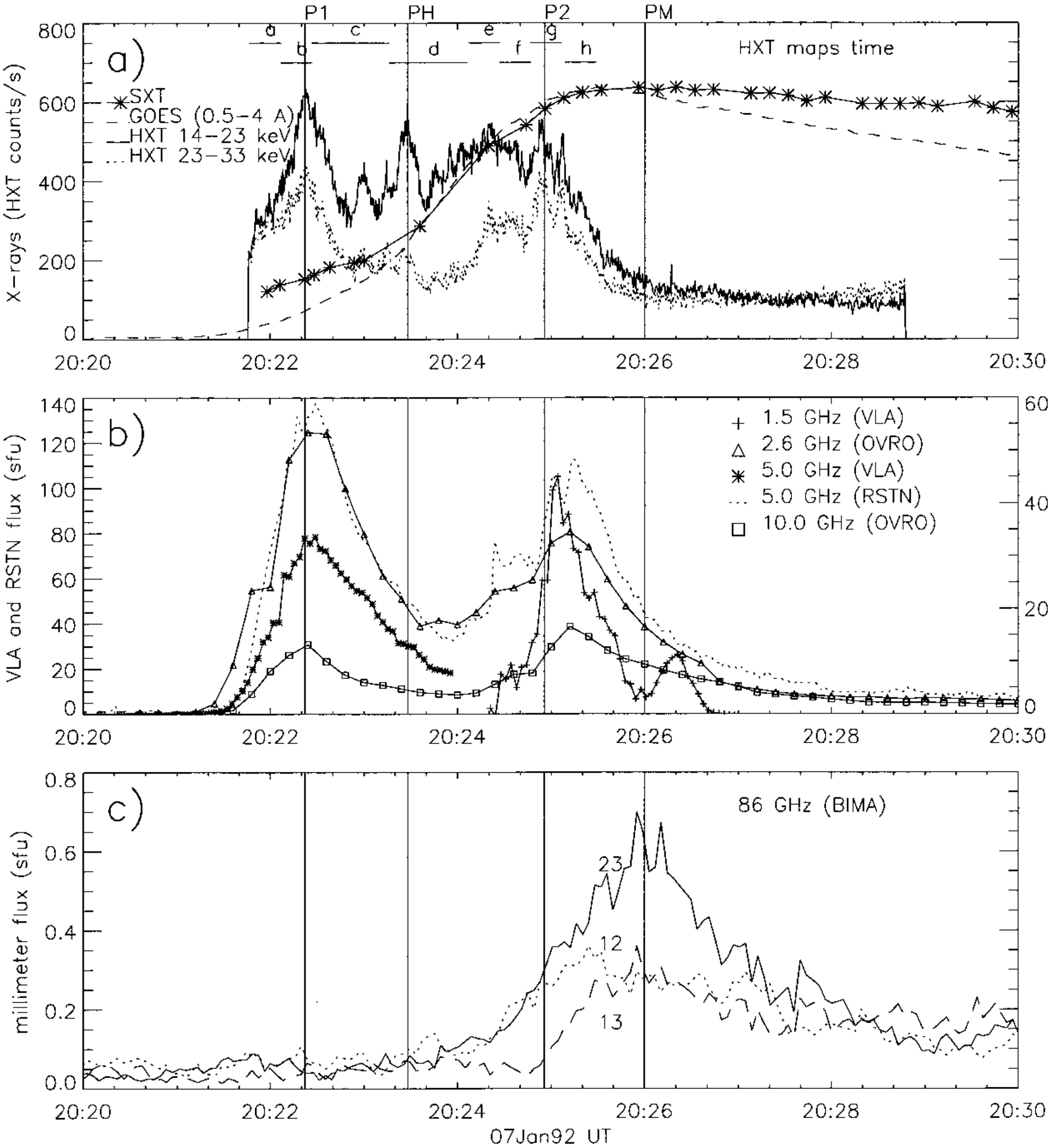

FIG. 4.—Time profiles of the emission detected at different wavelengths. (*a*) Soft (SXT and *GOES*) and hard X-ray (HXT 14–23 keV and 23–33 keV channels) data together with the time intervals of the X-ray maps; (*b*) microwave emission from the VLA, OVRO, and RSTN (*dotted line*); (*c*) millimeter flux as measured on BIMA's three baselines. The microwave data clearly show that the flare consisted of two main bursts; the first one peaked at P1, and the second peak occurred just after P2, when the hard X-rays peak. PH marks the intermediate peak seen in HXT LO channel. The maximum of millimeter emission occurred at PM.

4*b*. The microwave temporal evolution is very similar from 0.245 GHz (RSTN) to 14.0 GHz (OVRO), and the two main bursts, P1 and P2, are clearly seen. The peak at P1 lasts for ~ 70 s and is dominant for frequencies below 9.0 GHz, whereas the second burst, P2, becomes the main peak for frequencies above 10 GHz and lasts ~ 50 s. The microwave (>2 GHz) burst at P2 is delayed by ~ 10 s from the hard X-ray peak.

At the time of the observation, BIMA consisted of three antennas aligned on an east-west line, operating at a wavelength of 89 GHz (3.3 mm). Figure 4*c* presents the flux amplitude for the three baselines. Note that BIMA, which was pointing well away from the main flare site, detected no emission at the time of the first burst (P1). The millimeter emission starts to rise at the same time as the microwaves and hard X-rays rise toward P2; however, its peak, PM, occurs a minute later, at 2026 UT. The rise time is about equal to the decay time for the millimeter emission. The highest flux density comes from the shortest baseline (fringe spacing of 24″), which is sensitive to the largest spatial scales. Hence the emission region is resolved by the interferometer.

5. Hα OBSERVATIONS

On 1992 January 7, digitized Hα images were obtained at MSFC at 2000, 2002, and 2003 UT and every 2 minutes from 2024 to 2052 UT. In addition, there is continuous coverage on video from 2022:11 to 2034:55 UT.

The morphology of the Hα flare emission changes very little throughout the flare. Figure 5 shows the Hα image at the time of the first peak, P1, with sources A, B1, C, D1/D2, E, F, and G labeled according to Figure 1. The Hα picture bears a remarkable resemblance to the early SXT flare images, with bright sources at the same locations as SXT brightenings. After PH, the extended horizontal feature joining source G to E starts to dim. At P2, the morphology of the Hα sources is still the same as at P1. At this time, however, the Hα brightenings coincide with the brightenings in the HXT maps but not with those in the SXT maps (see Fig. 6*h* below), since the latter have changed. At no time is X-ray source B2 or H seen in the Hα photographs. Neither is the 1.5 GHz source J (discussed in § 7.2.2) observed in Hα.

6. X-RAY OBSERVATIONS (*YOHKOH*)

6.1. *SXT and HXT*

A time sequence of high-resolution SXT (2".5) images and HXT (5") maps made in the LO (14–23 keV) and M1 (23–33 keV) channels is shown in Figure 6. The HXT maps were integrated over 20 s except for intervals *c* and *d*, which were 50 s integrations to accumulate enough counts for adequate mapping. Nine different sources have been identified in the soft X-ray images throughout the flare, namely, A, B1, B2, C, D1, D2, E, F, and G (see Fig. 1 for source labels). SXT bright spots are indicative of hot plasma, at temperatures of $\sim(5–25) \times 10^6$ K. The HXT maps show hard X-ray emission from most of the same sources as in the LO and the M1 maps, with the following exceptions:

1. Source F could not be mapped in the HXT LO and M1 maps since it is at the edge of the field of view.
2. Curiously, source A is not seen in the HXT maps (discussed in § 8).
3. Source E is not present in the HXT LO maps and is very weak in the M1 maps.
4. Source J, seen in radio maps, is well outside the field of view of both full-resolution SXT and HXT images.
5. Source H is detected in hard X-rays but is not observed in the SXT images or in the Hα photographs.

The sources detected by each instrument are listed in Table 2 with the time at which they were observed, the location of the maximum of the source according to Figure 6, and the polarity of the underlying photospheric magnetic field (see Fig. 1).

We determined whether a source was a footpoint of a magnetic loop by comparing the soft and hard X-ray maps with the Hα images. A source is identified as a footpoint if there is a simultaneous Hα brightening at that position,

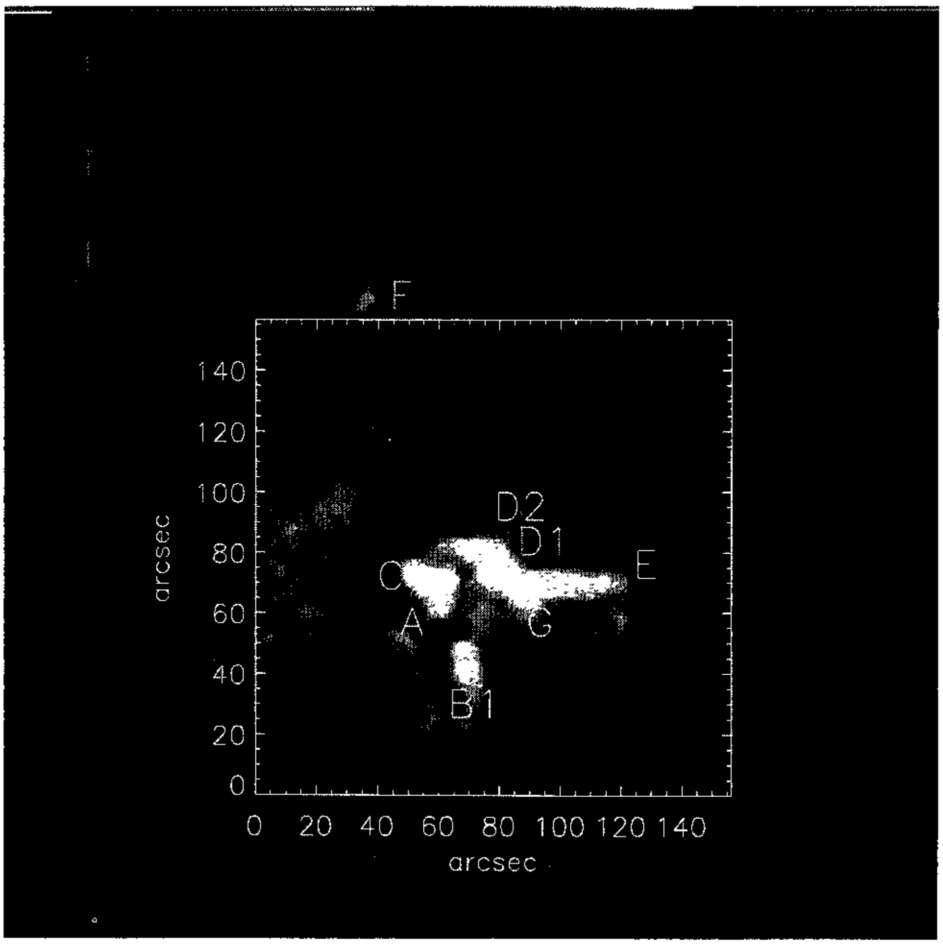

FIG. 5.—Hα image from MSFC at the time of the first peak, P1. The sources are labeled according to Fig. 1. The box represents the square field of view of the SXT full-resolution images.

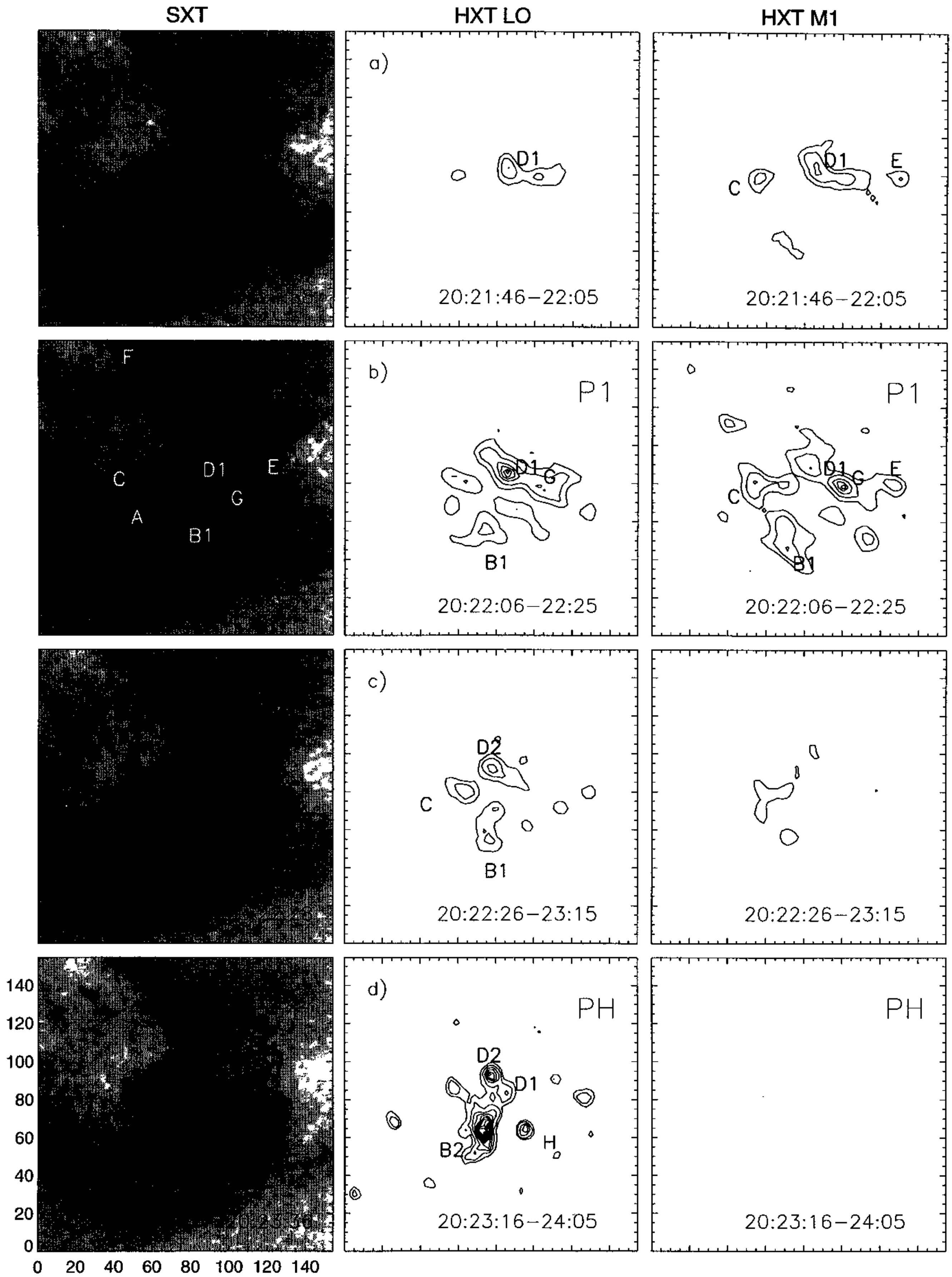

FIG. 6.—Time sequence of full-resolution images from SXT (*left*), HXT LO (*middle*), and HXT M1 (*right*) maps. The time of the images is shown at the bottom of each panel. The images suggest an intricate array of magnetic loops. The sources are labeled according to Fig. 1. The contour levels are the same within each HXT channel: 10%, 20%, 30%, 40%, 50%, 60%, 70%, 80%, 90%, and 100% of the maximum HXT emission in each channel.

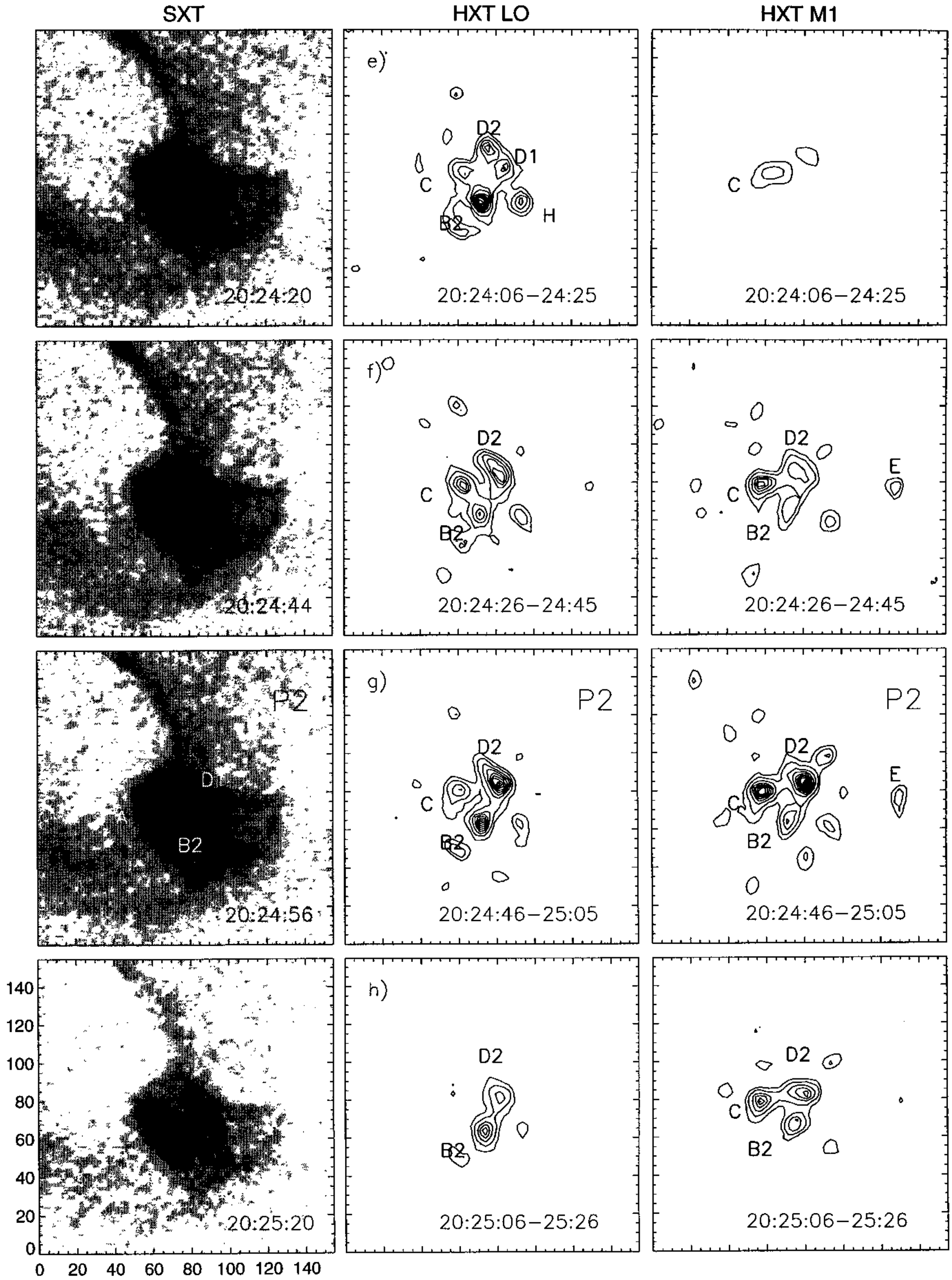

FIG. 6—*Continued*

since this indicates chromospheric heating. Thus sources A, B1, C, D1, D2, E, F, and G are footpoints of magnetic loops whereas sources B2 and H, not seen in Hα, are believed to be located near the tops of magnetic loops.

Magnetic loops are identified based on underlying magnetic polarity and simultaneity of loop footpoint emission. Sources B1 and F are the only footpoint sources overlying negative polarity (see Fig. 1). Two magnetic loops are clearly identified in the SXT images. A loop joining source B1 to D1/D2, hereafter loop BD, is seen early in the flare (Fig. 6*b*, *left*) whereas, from PH onward, a brighter compact loop connects source A to B1 (loop AB), with source B2 at its top (Fig. 6*f*, *left*). At P1, source G is the brightest source in the M1-channel map. This suggests that source G is connected to B1, the only negative-polarity footpoint nearby (loop BG). Loop BG, with loop-top source H, is shown by dotted lines in Figure 1. Since source C is also observed in the LO and M1 maps at P1, it is probably also connected to B1 (loop BC). Loops AB and BC seem to be two nested magnetic loops. The northern source F is likely connected to source C, source D1, or both.

Time profiles of the brightest sources seen in the SXT and HXT maps are presented in Figure 7. The top part of each panel shows the spectral index γ, i.e., the exponent of the power-law fit to the hard X-ray spectrum,

$$I(h\nu) = a(h\nu)^{-\gamma} \text{ photons s}^{-1}\text{ cm}^{-2}\text{ keV}^{-1} , \qquad (1)$$

for each source calculated from the HXT maps (discussed below). The light curves were obtained by totaling the brightnesses within the boxes shown in the top left panel of Figure 7 superposed on an SXT image. These same boxes were used in the calculation of the physical parameters and power-law index, γ, of each source. The boxes are the same for the SXT and HXT maps and remain fixed throughout the flare. Each box was centered on the average position of the peak emission of the source as determined from SXT, HXT LO, and HXT M1 maps. The size of each box was chosen such that there was no overlap and the contribution from adjacent sources was minimized. A source was considered to be distinct when its centroid was more than 10″ away from any other source, since the resolution of HXT maps is $\sim 5''$.

The temporal evolution of the flare's morphology is as follows: There was some preflare heating at site D1, as can be seen from its SXT time profiles (Fig. 7). Moreover, source D1 was already bright in preflare SXT maps (see Fig. 3). During P1, the bright footpoints of loops BC, BD, and BG are observed, namely, sources B1, C, D1, and G. The M1-channel emission is dominated at this time by source G. Loop BD is bright in soft X-rays. Source A is very weak at this time. At PH, the LO-channel maps differ significantly from the M1 maps (Figs. 6*c*–6*e*) since there is very little emission in the M1 maps. The loop-top source B2 dominates the HXT LO images during PH. The LO maps also show source H, presumably a loop-top source, and footpoint source B1. Loop AB is seen in soft X-rays to begin to fill in with hot plasma. Source A is the brightest soft X-ray source at PH. At P2, there are mainly three sources visible in the hard X-ray maps, namely, B2, C, and D2 (Figs. 6*f*–6*h*). Three sources are also seen in the SXT images (A, B2, and D2), although D2 quickly fades in importance compared to A and B2. The SXT images at P2 clearly outline the loop joining A and B1, and the strongest soft X-ray source now is B2 instead of source A. No hard X-ray emission was observed from source A. During the decay phase, soft X-rays from source A decay faster than those from sources B1 and B2. By PM, all the hard X-ray emission has ceased and the soft X-ray images are similar to SXT Figure 6*h* (*left*), showing only a strong AB loop. Source B2 is still the brightest soft X-ray source at PM.

Images were made in the M2 (33–53 keV) channel during P1 and P2. Because of the low count rates, the integration time needed to make a map was considerably longer (over a minute). The M2 map, which includes P1 (2021:46 UT to PH) shows sources at D1 and possibly at B2. The second M2 image (around P2) shows D2 as the brightest source, with weaker sources at C and B2.

Maps of soft X-ray temperature and emission measure (EM) can be obtained for each pixel in the high-resolution SXT images by taking the ratio of the beryllium (^{119}Be) and aluminum (^{12}Al) filter images (Vaiana, Krieger, & Timothy 1973; McTiernan et al. 1983). The temperature, emission measure, and ambient density calculated for sources A, B1, B2, C, D1, D2, and G at P2 are listed in Table 3. The high emission measure regions (indicative of high density) coincide with the bright spots in the SXT images. The regions of highest temperature are found on the edges of the high-EM regions; this same pattern has been reported by McTiernan et al. (1993). The average temperature and total emission measure for the whole flare from the maps are in excellent agreement with the values derived from *GOES* data. The temperature maps show the presence of a single source, B2, from P1 to P2 located at the top of the soft X-ray loop AB. Its temperature reaches a maximum of 2.2×10^7 K at 2024 UT.

Spectra were made by using the three lower HXT energy-channel (LO, M1, and M2) count rates, spatially summed over the entire flare (the count rates in the high channel, 53–93 keV, were too low). Figure 8 shows the temporal evolution of the spectral index, γ. The photon spectrum of the LO/M1/M2 channels (*asterisks*) at the time of the first burst, P1, has a slope of ~ 4.2. This spectral index steepens to 7–8 after PH and stays steep until ~ 2024 UT. Then the spectrum becomes hard again by 2024:15 UT, and at P2, $\gamma = 3.7 \pm 0.3$. The spectral index calculated from the M1/M2 channels (*triangles*) shows a very different behavior, remaining low at $\gamma \sim 4$–5 throughout this period, and coincides with the index calculated from the LO/M1/M2 channels from 2024:30 UT onward. This variation in spectral index with energy implies that the spectrum fits a single power law from 14 to 53 keV except between 2023:30 and 2024:15 UT, when there is a break in the spectrum with a much steeper power-law index at low energies.

6.2. *X-Ray Spectroscopy* (*BCS*)

The Bragg Crystal Spectrometer observes the Fe XXV, Ca XIX, and S XV line complexes, with no spatial resolution. The instrument and line-fitting procedures are described in Appendix A (§ A4). The BCS data implied approximately a 5 minute rise time and a 20 minute decay time for plasma hotter than 7×10^6 K, consistent with the *GOES* and SXT time profiles in Figure 4.

The BCS S XV and Ca XIX spectra taken before 2022 UT show a slightly enhanced emission at temperatures less than 7×10^6 K and an emission measure of $\sim 5 \times 10^{47}$ cm^{-3}. In Figure 9, BCS spectra (*histograms*) are shown together with the spectral fits (*solid lines*) for Ca XIX at times P1 (*top*) and P2 (*bottom*). The dotted lines represent the stationary line

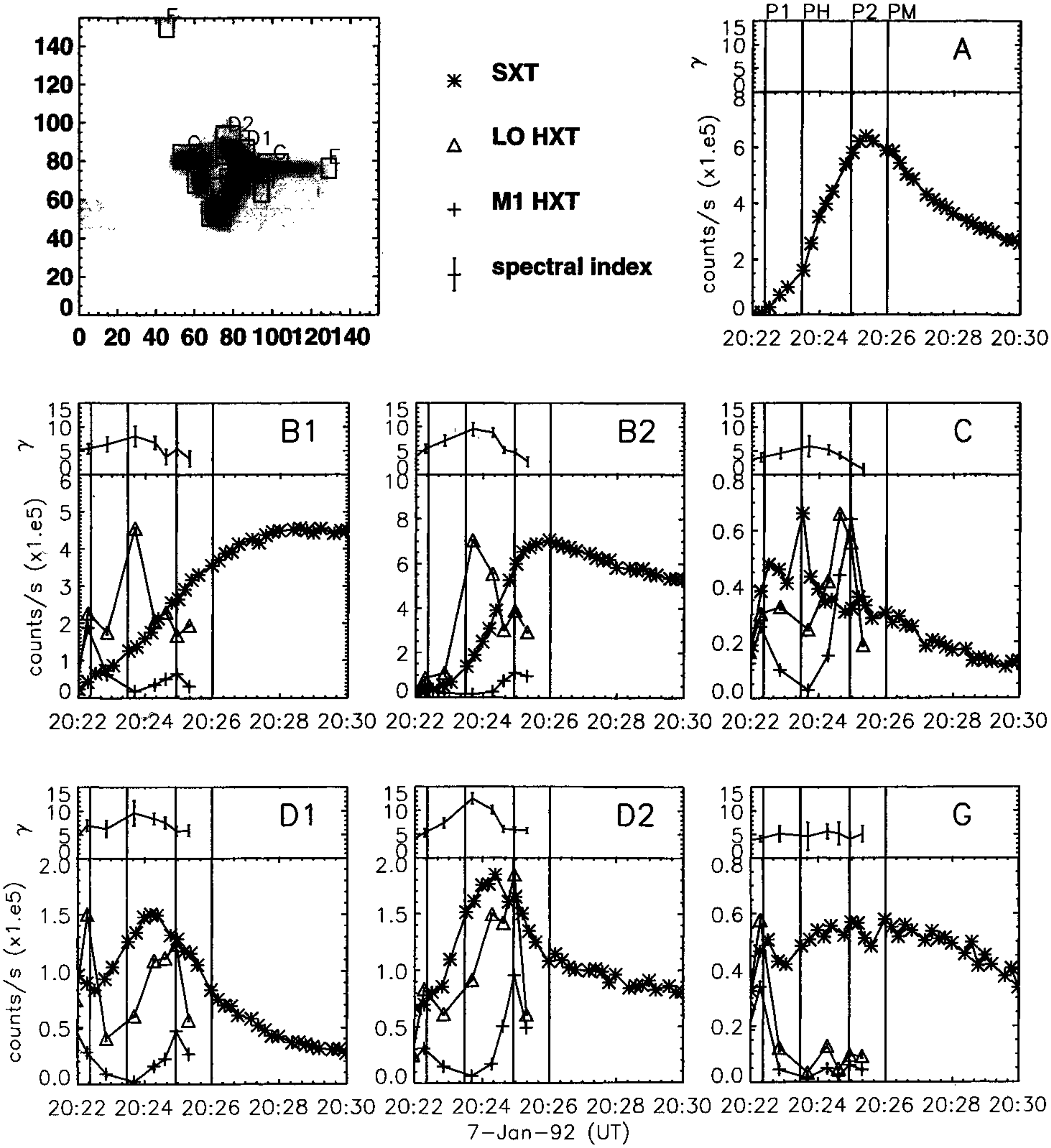

FIG. 7.—Time profiles of soft and normalized hard (LO and M1 channels) X-ray emission of the individual sources. The boxes used in calculating the light curves are shown in the upper left panel. Also plotted at the top of each panel is the spectral index for each source, calculated from HXT maps.

profile. At P1, the observed profile is very asymmetric, shifted toward the blue end of the spectrum, indicating the presence of upward-flowing plasma. Large asymmetries of line profiles are observed in all three BCS channels for the peak P1 of this flare, but not at P2.

The electron temperature, emission measure, and line width of the stationary component, plus emission measure and average upflow velocity of the moving component, were derived by a fitting procedure given by Fludra et al. (1989). A summary of the derived parameters is given in Figure 10. After P1, the Ca XIX flux started to increase more rapidly, reaching a maximum at about P2 (Fig. 10*a*).

To determine the average upflow velocity, the position of the rest component during the rise phase is assigned the

TABLE 3

PHYSICAL PARAMETERS AT P2

	SXT			HXT				OVRO				ENERGY (10^{29} ergs)		
SOURCE	n_{10}	T_6	EM_{49}	γ	Population	δ_X	$n_e(E > 10)$	δ_r	$n_e(E > 10)$	r	B	ϵ_{th}	$\epsilon_{inj}(E_0)$	ϵ_{20}
A	6.6	13.5	0.41	...	...	...	...	4.1	10^8	3	500	2.4	...	...
B1	3.5	16.4	0.19	5.4	inst	4.9	3.8×10^6	...	...	...	...	...	...	...
					accel	6.9	2.5×10^7	...	...	...	...	2.3	2.1 (14.2)	0.28
B2	5.1	19.2	0.33	4.7	inst	4.2	8.4×10^6	4.9	10^8	6	370	2.5	2.5 (15.8)	0.89
					accel	6.2	6.6×10^7	...	...	...	...	...	...	...
C	2.2	13.6	0.08	2.5	inst	2.0	1.7×10^6	...	...	...	...	...	...	...
					accel	4.0	1.7×10^6	...	...	...	...	0.96	0.79 (15.0)	0.28
D1	2.2	14.2	0.05	5.7	inst	5.2	1.7×10^7	...	...	...	...	...	...	...
					accel	7.2	7.9×10^7	...	...	...	...	0.34	0.58 (19.5)	0.49
D2	1.8	16.7	0.08	6.0	inst	5.5	4.6×10^7	...	...	...	...	...	...	...
					accel	7.5	1.8×10^8	...	...	...	...	0.91	1.3 (21.0)	2.0
G	1.2	11.7	0.02	4.0	inst	3.5	2.6×10^6	...	...	...	...	...	...	...
					accel	5.5	3.7×10^6	...	...	...	...	0.11	0.47 (15.0)	0.15

NOTES.—Inferred physical parameters at P2 from the soft X-ray data (ambient density n_{10}, in cm^{-3}, electron temperature T_6, in millions of kelvins, and emission measure EM_{49}, in units of 10^{49} cm^{-3}); the hard X-rays [photon spectra power-law index, γ, electron energy distribution power-law index, δ_X, and density of energetic electrons, $n_e(E > 10$ keV), and whether the electron population was assumed to be the instantaneous or the accelerated one]; and the microwave emission (spectral slope of electron energy distribution, δ_r, electron density in cm^{-3}, source radius r, in arcseconds, and magnetic field strength B, in gauss). The three last columns list the maximum thermal energy inferred for each of the X-ray sources (ϵ_{th}), the total energy injected at each source site by the energetic electrons (ϵ_{inj}), and the total injected energy for electrons with $E > 20$ keV (ϵ_{20}).

position determined from data taken during the decay. Spectral data taken at 2021:46 UT (almost a minute before P1) provide the first clear evidence of upflowing plasma through enhanced blue-wing emission. The upflow velocity at this time was $\sim$200 km s^{-1} and remained at this value through PH. At 2024 UT, it increased to $\sim$350–370 km s^{-1} for about 1 minute before returning to the $\sim$200 km s^{-1} level (Fig. 10*b*). This increase in upflow velocity is believed to be real and is perhaps related to the activation of a new loop, resulting in a new upflow. The turbulent velocity, determined from the Ca XIX spectra, reached a maximum of $\sim$120 km s^{-1} during the rise phase, falling to 60–80 km s^{-1} in the decay phase.

An electron temperature of 1.7×10^7 K was derived from Fe XXV observations at the time of maximum upflows, 2024:10 UT (Fig. 10*c*). This temperature is an average over

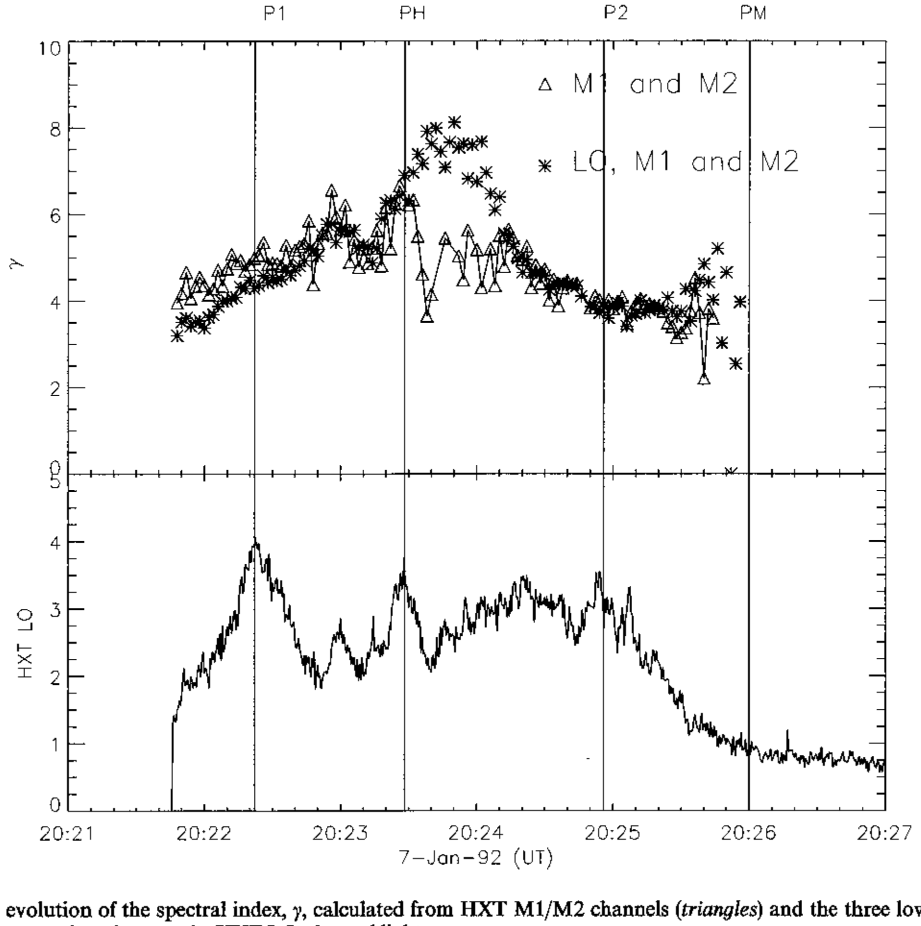

FIG. 8.—*Top*, temporal evolution of the spectral index, γ, calculated from HXT M1/M2 channels (*triangles*) and the three lower channels (LO/M1/M2; *asterisks*) spectra fitted by a power law; *bottom*, the HXT LO-channel light curve.

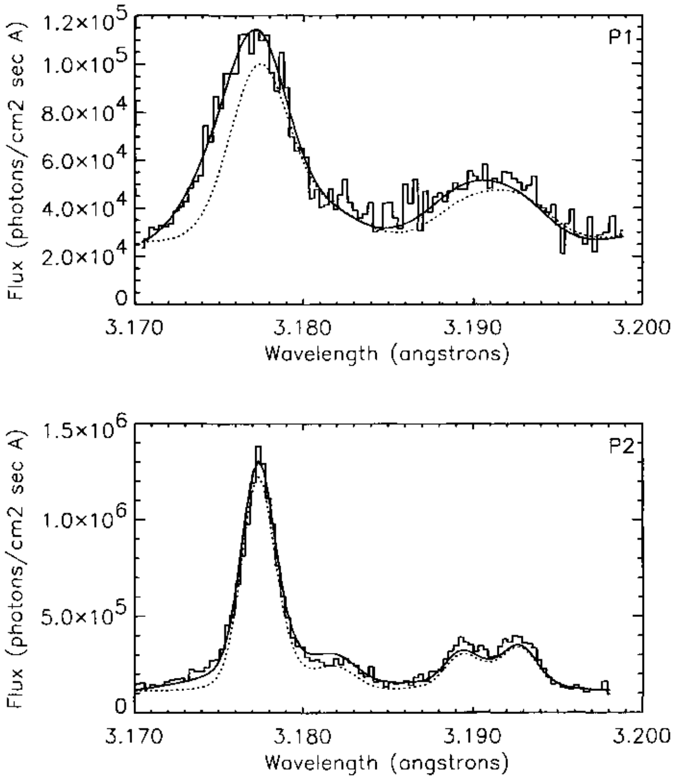

FIG. 9.—Ca XIX data (*histograms*), summed over 24 s intervals, plus the fitted theoretical spectra (*solid lines*) for two time periods throughout the 1992 January 7 flare. *Top*, during the impulsive phase shortly after P1; *bottom*, at flare maximum at P2. The dotted line represents the "stationary" component only.

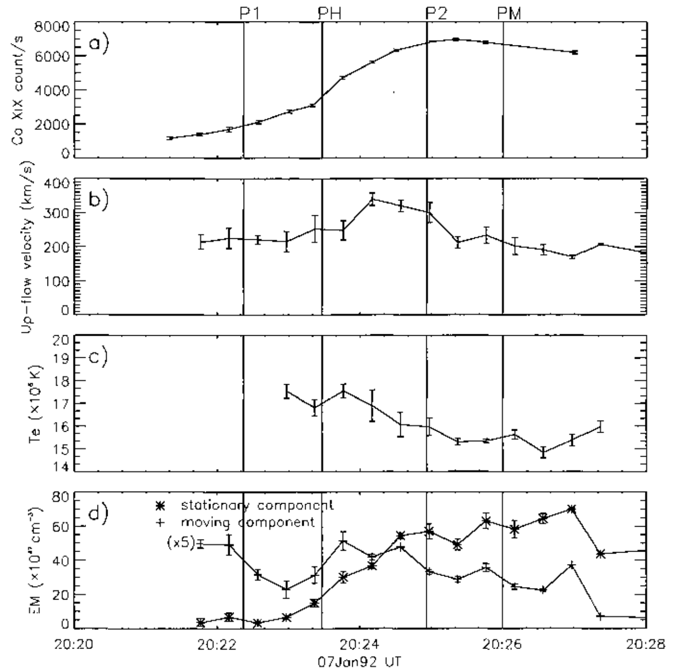

FIG. 10.—Summary of the derived parameters for the 1992 January 7 flare. (*a*) Ca XIX light curve; (*b*) upflow velocity of the moving component; (*c*) electron temperature from Fe XXV; (*d*) the emission measure of the "stationary component" and the "moving component" (the latter multiplied by 5).

the emitting region, and thus it is lower than the maximum spatially resolved SXT temperature measurements.

The temporal evolution of the "moving plasma" emission measure, EM_M, multiplied by 5, and the "stationary" plasma, EM_S, are plotted in Figure 10*d*. The largest value of EM_M/EM_S is ~ 2.5, found in a spectrum beginning at P1 and integrated for 24 s. The corresponding average upflow velocity at this time is 200 km s^{-1}. This ratio becomes less than unity after 2023 UT and is ~ 0.10 at PM.

7. RADIO OBSERVATIONS

7.1. *Radio Solar Telescope Network–Sagamore Hill*

The RSTN data consist of total-power time profiles from the Sagamore Hill station at 0.245, 0.410, 0.606, 1.415, 2.695, 4.995, and 8.8 GHz. The RSTN and OVRO time profiles at 2.6, 5.0, and 8.8 GHz are very similar (see Fig. 4). The RSTN data, however, have higher temporal resolution (1 s), so that the second burst (P2) is resolved into three peaks, which are also seen in hard X-rays by HXT (especially in the M1 channel). At 5 GHz, the first of these peaks, at 2024:40 UT, measures 70 sfu. The second peak, shortly before 2025 UT, reaches 105 sfu, and the third, at 2025:12 UT, peaks at 115 sfu.

7.2. *Very Large Array*

The VLA data show two bursts, P1 and P2. From 2021 to 2024 UT, the VLA was observing at 5 GHz. It then switched to 0.33/1.5 GHz while peak P1 was still decaying, and immediately the rise to peak P2 (of ~ 100 sfu) began at 1.5 GHz. The VLA data were reduced by using the standard AIPS data reduction package. For a description of the interferometer, see Appendix A (§ A5).

7.2.1. 5.0 GHz

The VLA detected three distinct sources at 5 GHz (2021–2024 UT) during burst P1. Figure 11 shows an overlay of the 5 GHz sources on an SXT high-resolution image at P1 (Fig. 6*b*). The radio images have a resolution of $3''.9 \times 3''.4$. All three sources appear to be extended at this resolution and reach sizes comparable to the largest structures "visible" to the VLA (18" at 5 GHz). Therefore it is likely that the VLA images do not accurately represent the total flux density in the flare region. This may explain the factor of ~ 2 discrepancy between the flux densities reported by RSTN and the VLA (Fig. 4*b*). The main source is close to source A (the offset of 5" is about the uncertainty of the radio-on-SXT overlay), which also has an Hα counterpart. Another source located $\sim 100''$ to the north, over the strong trailing sunspot of AR 6993, coincides with SXT source F. There is also Hα emission from this site. The third source, H, does not have an Hα counterpart. This location corresponds to feature H seen in HXT LO maps.

Figure 12 shows the temporal evolution of the total flux density of each of the three sources in right (RCP) and left (LCP) circular polarization, together with Stokes $V = \mathrm{RCP} - \mathrm{LCP}$ at 3.3 s temporal resolution. The three sources appear to brighten almost simultaneously, but source H reaches its maximum 15 s earlier than the others. Source F decays more slowly than the other two sources. Source A is strongly RCP polarized and is the dominant source in the RCP maps. Sources A and F show a very similar evolution in the LCP and RCP flux. Comparison of the sense of radio polarization with the underlying photospheric magnetogram indicates that both sources A and H

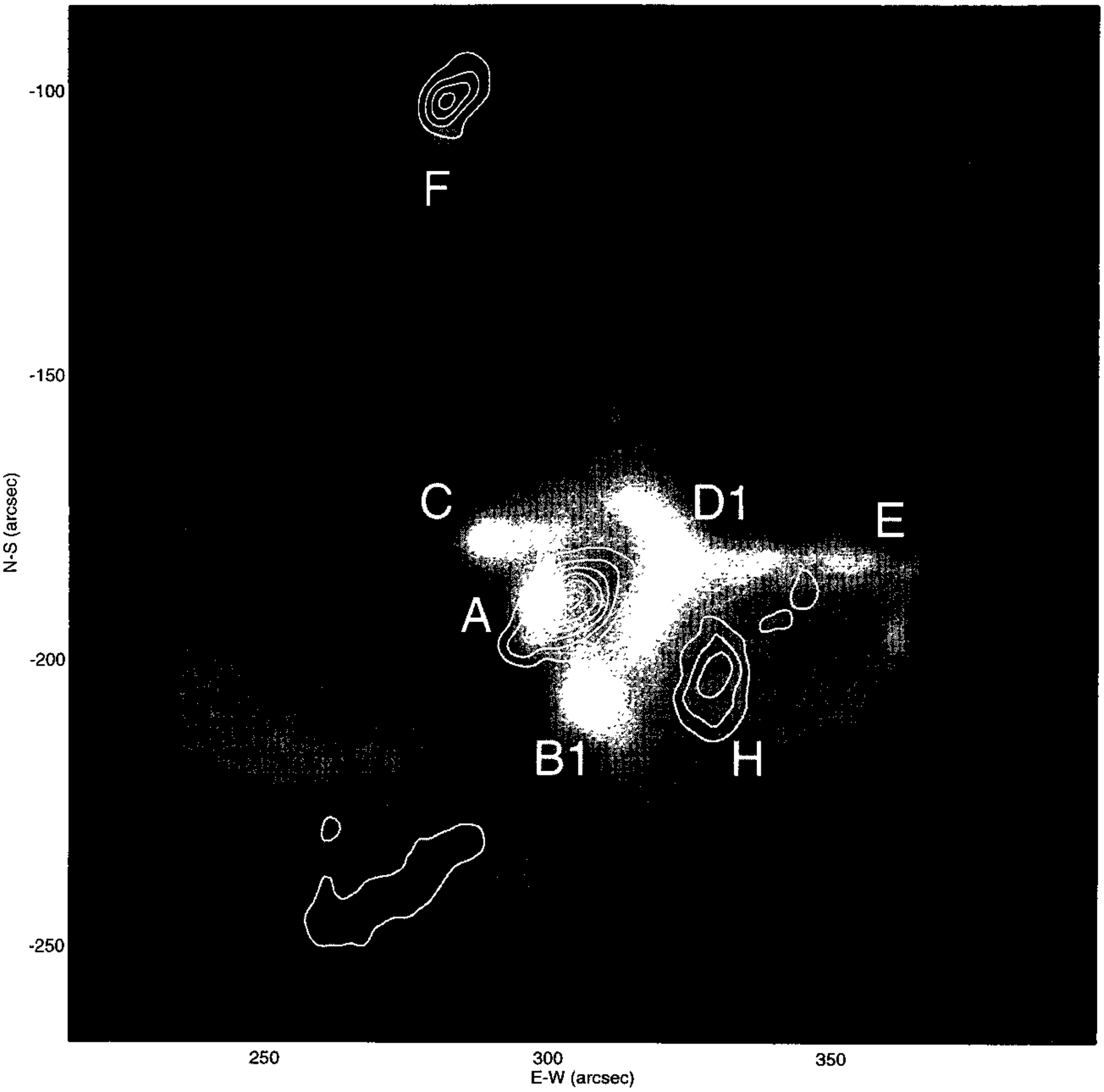

FIG. 11.—VLA 5.0 GHz contours superposed on an SXT high-resolution image, at the time of the first peak (P1). The contours are at 20%, 35%, 50%, 65%, 80%, and 95% of the maximum flux density, 0.76 sfu beam^{-1}, and the beam is 3".9 × 3". The peak brightness temperature is ~5 × 10^7 K.

are polarized in the sense of the X-mode, as would be expected for gyrosynchrotron emission.

7.2.2. 1.5 GHz

By the end of the 5 GHz scan at 2024 UT, the first radio burst (P1) has virtually ended and the flux densities are close to preflare levels. The VLA began to take data at 1.5 GHz at 2024:22 UT, when a second burst was found to be in its rise phase. Figure 13 shows the maps near the 1.5 GHz peak in RCP and LCP, overlaid on the KPNO magnetogram. Because of the limited (u, v)-plane coverage (u and v being the spatial frequencies), there is little confidence that all the fine structure of the sources seen in these images is real, but the overall low-resolution structure is real. The main emission at 1.5 GHz came from a source (hereafter source J) over the trailing end of AR 6994, which reached a total flux of ~150 sfu in RCP. This source was not detected by OVRO, SXT, or in Hα (the source was outside the field of view of HXT). Since source J was not detected by OVRO at higher frequencies (≥2.6 GHz), it must have had a very steep spectrum. The OVRO total-power measurement at ~2 GHz is only ~44 sfu in RCP whereas the 1.5 GHz VLA flux is ~170 sfu. Even though this source was located within the BIMA primary beam, the millimeter emission is probably not associated with source J since it has no signature at microwave frequencies higher than 2.6 GHz.

Note that the contour levels are different in the two panels of Figure 13. Source J was nearly 100% RCP polarized. With respect to the underlying negative magnetic polarity, it was polarized in the sense of the O-mode. The main 1.5 GHz peak lasted ~1 minute; the peak brightness temperature was ~1 × 10^9 K. There may have been some structure within source J (notably, a north-south extension).

By PM, source J is fading. At this time, a new source appears to the northwest over the sunspot at the trailing

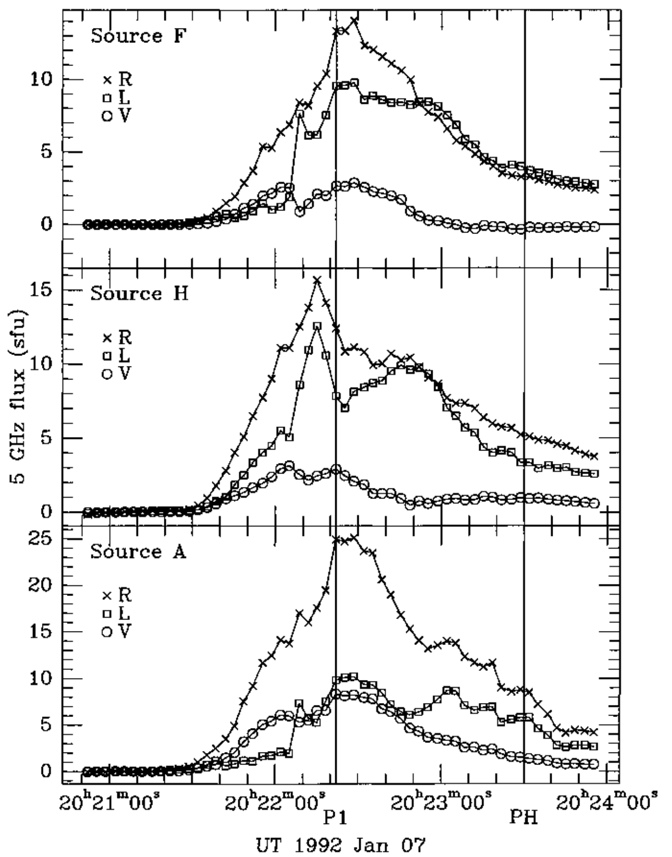

FIG. 12.—Time profile of the 5.0 GHz VLA total fluxes of the three sources seen in Fig. 11. Plotted are right-circular polarization (*crosses*), left-circular polarization (*squares*), and $V = \mathrm{RCP} - \mathrm{LCP}$ (*circles*). Note that the strongest source, A, is strongly RCP polarized.

end of AR 6993, in exactly the same location as source F, seen by the VLA at 5 GHz and in SXT images. Time profiles of sources F and J are shown in Figure 14 for RCP, LCP, and $V = \mathrm{RCP} - \mathrm{LCP}$. Source F brightens rapidly, peaking 10 s after P2 and at PM. Source J also is double-peaked: the first peak is 5 s after P2, and the second ~ 20 s after PM; the later peak lasted 30 s. The two sources are $\sim 150''$ apart. The bottom two panels of Figure 13 show source F at an early stage, before J has rebrightened. There is also an extended source at the location of source A, which may be thermal emission from postflare loops (brightness temperature of order 3×10^7 K). Its temporal evolution is similar to that of source J (Fig. 14). These loops are not visible earlier, largely as a result of the limited dynamic range of the images, and the signal-to-noise ratio is not adequate to analyze this source in great detail. The temporal evolution of RSTN 1.415 GHz emission is very similar to the total flux density from the VLA 1.5 GHz data. The small secondary peak seen by the VLA, ~ 20 s after PM, was also detected by the Sagamore Hill telescope.

7.3. *Owens Valley Radio Observatory*

On 1992 January 7, OVRO observed the flare at 45 frequencies, ranging from 1 to 18 GHz, with a temporal resolution of 12 s. The data were taken in right- and left-circular polarization. The total power from one of the 27 m antennas is also available. The OVRO array is described in Appendix A (§ A6), together with the mapping technique used. Because of the problems discussed in this appendix, we will concentrate our discussion on the LCP maps.

The LCP maps made at P1 vary substantially throughout the frequency range. At low frequencies, the dominant source is close to source F whereas, at midfrequencies, the sources are all located in the central region, close to sources A and B2. Only one source, F, is visible in the ≥ 9 GHz maps. Note that the VLA 5 GHz images (which agree with the OVRO map at 5 GHz made at P1) were taken during the first burst, P1, while in this section we will discuss mainly the sources detected on the OVRO maps made during the second burst, P2, which could be mapped because of its simpler morphology.

Figure 15 shows the single-frequency LCP maps, from 3.4 to 13.2 GHz, at the time of the second burst peak, P2. The SXT and HXT LO maps at P2 are shown in the top row of Figure 15 for reference. The images at frequencies $\nu \leq 7$ GHz show source B2 while, at higher frequencies, the main source is located at A. At midfrequencies, both sources A and B2 can be distinguished. Because the observation took place very close to the winter solstice, the beam is quite elongated (shown in the top left corner of each panel), causing the shape of the sources to also be elongated. Both sources are essentially unresolved (see below). The dynamic range of the maps is 10:1, and no source with a flux density less than 20% of the main source can be unambiguously detected. The two sources are separated by only $20''$ and could not be resolved in RCP (see Appendix A, § A6). Comparison with magnetograms shows that source A is over positive polarity whereas source B2 overlies negative polarity (Fig. 1). The magnetic field intensity is stronger at A (500–1000 G) than at B2 (~ 500 G). Source A is thought to be a footpoint of loop AB, whereas B2 is located at the top of this loop. The sources are on each side of the neutral line that runs between them.

Before the spectrum of a source can be constructed, the size of the emitting region needs to be determined. The flux density and size of the source were determined by fitting a Gaussian source to the brightest source in the map. This fit was then subtracted from the map, and the next brightest source was modeled in the same way. This procedure provides both the flux density and the size of the modeled sources. The sources are unresolved in both the direction of the beam's major and minor axes. Hence, at P2, the upper limit to the diameter of source A is $6''$, and $10''$ for source B2. This is consistent with the VLA 5 GHz images.

The total-intensity spectrum is obtained by multiplying the LCP flux by the polarization of the source. The polarization data are obtained from the total-power data of antenna 1. The maximum polarization of the sources at P2 is $\sim 35\%$ (RCP) for source A and 50% for source B2. The polarization becomes highly uncertain above 9 GHz as a result of calibration problems; we thus assumed that source A has the same polarization as B2 at these high frequencies.

The spectra from the single-frequency maps for the two sources are shown in Figure 16. The two spectra are very similar except for their turnover frequency: source B2 has its spectrum peaking at 5.4 GHz whereas source A peaks at 9.0 GHz. At P2, the peak brightness temperature of source B2 is $(3.7 \pm 0.4) \times 10^7$ K, and $(2.6 \pm 0.3) \times 10^7$ K for source A. The solid and dashed lines are models for sources A and B2, discussed in § 8.2, whereas the dotted-line model is discussed in § 8.3.

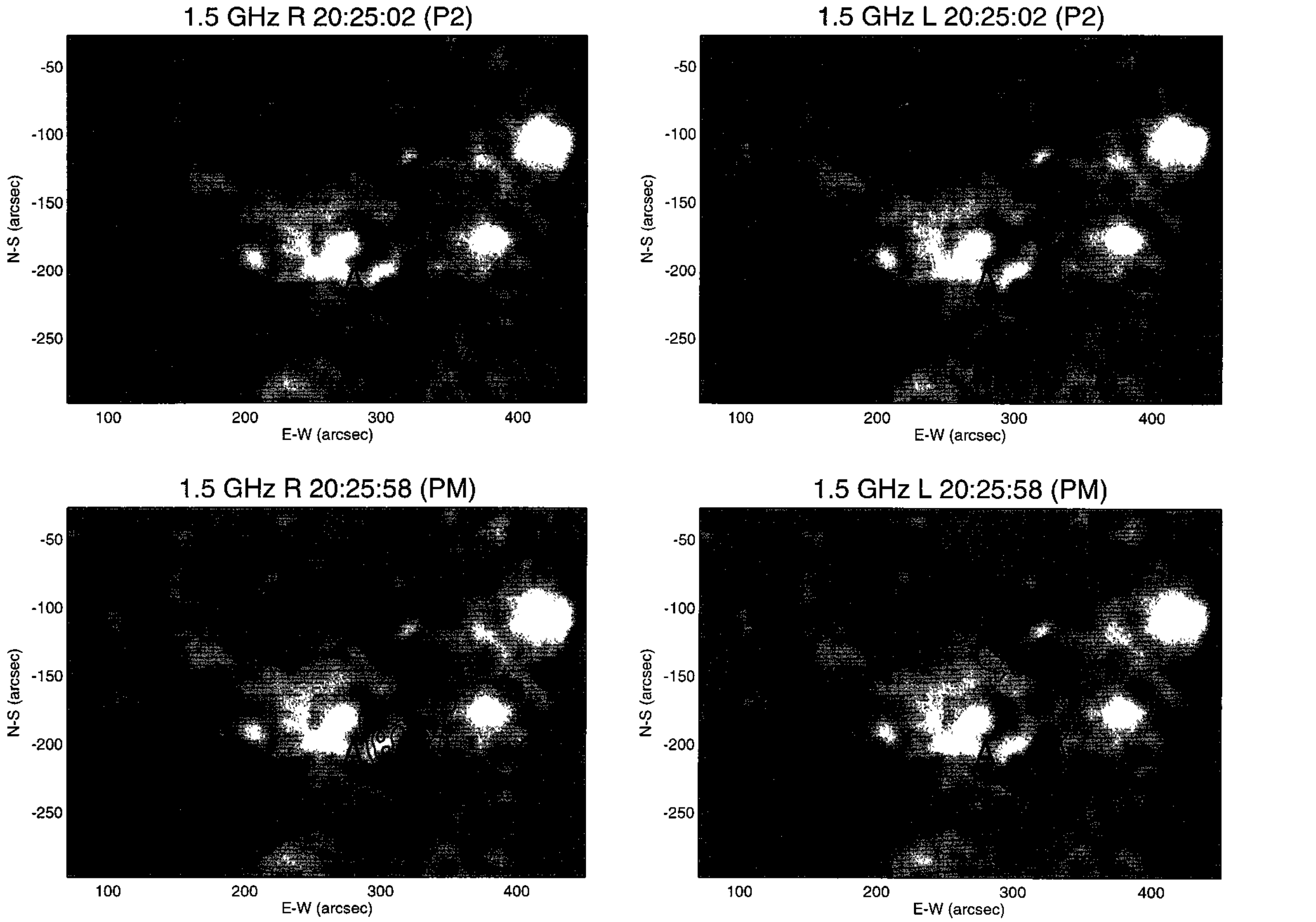

FIG. 13.—VLA 1.5 GHz maps overlaid on the KPNO magnetogram (Fig. 2, *bottom*), in RCP (*left*) and LCP (*right*). The two top panels show the 1.5 GHz sources at P2 whereas the bottom ones show the same region at PM. The contour levels are 2%, 3%, 4%, 6%, 8%, 10%, 12%, 16%, 20%, 24%, 32%, 40%, 48%, and 64% of 0.8 sfu (*top left*), 0.25 sfu (*top right*), and 0.6 sfu (*bottom*).

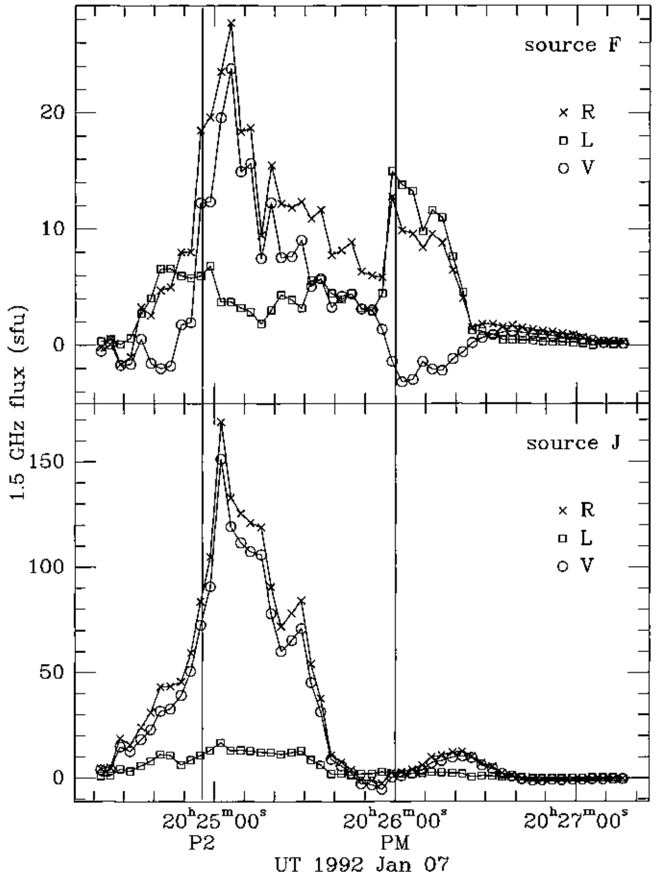

FIG. 14.—Time profile of the 1.5 GHz VLA total fluxes of the two sources, F and J, seen in Fig. 13. "R" and "L" stand for right- and left-circular polarization, respectively, and V = RCP − LCP.

Throughout the evolution of the flare, the total-power spectra remained flat for frequencies below 5 GHz, in contrast to the spectrum of the individual sources. Note that the total-power data for these low frequencies are spatially integrated over the whole active region. Both the total-power and map spectra agree at $\nu > 5.0$ GHz. The fact that the total-power flux density at $\nu \leq 5.0$ GHz is higher than the total flux density determined from images suggests the presence of large extended structures, i.e., on scales larger than the shortest baseline spacing (30″). When structures exceeding 30″ in size are present, they will not be "seen" by the interferometer, but do show up in the total power of a single antenna. These could, for example, be the long loops, arcminutes in size, seen in *Yohkoh* soft X-ray images (e.g., Fig. 3).

7.4. *BIMA Millimeter Observation*

BIMA, operating at 86 and 89 GHz (3 mm), did not detect any emission at P1 (Fig. 4*c*). The millimeter emission shows a smooth rise, starting around PH, which peaks at PM (about a minute after P2, the second microwave emission peak), and decays gradually until 2028 UT. The millimeter flux density reached 0.7 sfu at the shortest baseline. BIMA was pointing $\sim 110''$ away from the main flare site (sources A, B1, B2, etc.). Since the interferometer's primary beam is $\sim 2'.3$, the main flare site was outside its field of view. The primary beam is such that a source 110″ away from the pointing center would be detected at $\sim 16\%$ of its true flux. Thus, if the flux detected by BIMA originated from a source at the same position as the sources seen by the other instruments, then the millimeter radiation emitted by this source is ~ 2.5 sfu at P2 (plotted in the microwave spectrum of Fig. 16) and 4.4 sfu at PM.

On the other hand, the millimeter emission might have been produced by electrons accelerated by the flare at its main site of emission that then traveled the east-west loops (seen in Fig. 3) to where BIMA was pointing, $\sim 110''$ away from the main flare site. The time required for an electron with a velocity of one-third the speed of light to travel the aforementioned distance is ~ 1 s, far less than the delay of almost a minute between the millimeter peak, PM, and the second microwave/hard X-ray burst, P2. However, there was no evidence for this in the hard X-ray, microwave, or Hα observations.

8. DISCUSSION

In this section, we discuss the energy input and deposition, the physical parameters of the individual flare sources, and the millimeter-wave emission mechanism based on a comparison of the 86 GHz and soft X-ray emissions. The temporal evolution of the 1992 January 7 flare can be divided into three particle-acceleration phases and a thermal phase.

The first particle-acceleration phase, which occurred at P1, is purely nonthermal and impulsive. The hard X-rays at this time show where the accelerated electrons reached the footpoints of magnetic loops at B1, C, D1, and G. Source G is the brightest source in the HXT M1 map. The coronal source H, thought to be located at the top of loop BG, is observed by the VLA at 5 GHz to peak ~ 7 s before P1. Some weak emission from H is barely visible in the HXT maps during P1.

The phase PH is characterized by hard X-ray emission with a steep energy spectrum (Fig. 8). Since very few electrons were accelerated to high energies, no microwave emission was observed at this time. During PH, BCS detected enhanced blueshifted emission of the Ca XIX line. Presumably, the electrons accelerated at PH precipitated into the chromosphere, heating and evaporating the chromospheric plasma to fill loop AB. Moreover, the photon spectral index, γ, measured from the three lower HXT channels (LO/M1/M2) at PH is consistent with that obtained from only the M1/M2 channels (both $\gamma \sim 5$–6), showing that the hard X-ray emission is power-law and therefore likely to be nonthermal at PH. After PH, the two spectral indices differ: $\gamma \sim 8$ from the LO/M1 and $\gamma \sim 5$ from the M1/M2 channels, which suggests significant thermal contribution to the spectrum. During PH, source B2 is very strong in the HXT LO map (Fig. 6), and the SXT temperature maps show a single source at B2, which reaches a maximum temperature of 22×10^6 K at 2024 UT.

During phase P2, the loop-top source B2 and footpoint sources C and D2 are detected in the hard X-ray maps. Thus, at this time, the energetic electrons impinge at footpoints C and D2 (Fig. 6). Source B2 is simultaneously observed in microwave and soft and hard X-ray maps while source A is seen in microwave and soft X-ray images only. Since no microwave sources are observed at site C or D1/D2, the coronal magnetic fields there are probably too weak to produce detectable microwave emission. The magnetic field strength at the coronal source B2 and at source A, as well as other spectral parameters, can be estimated by modeling the spectrum of the microwave sources. The

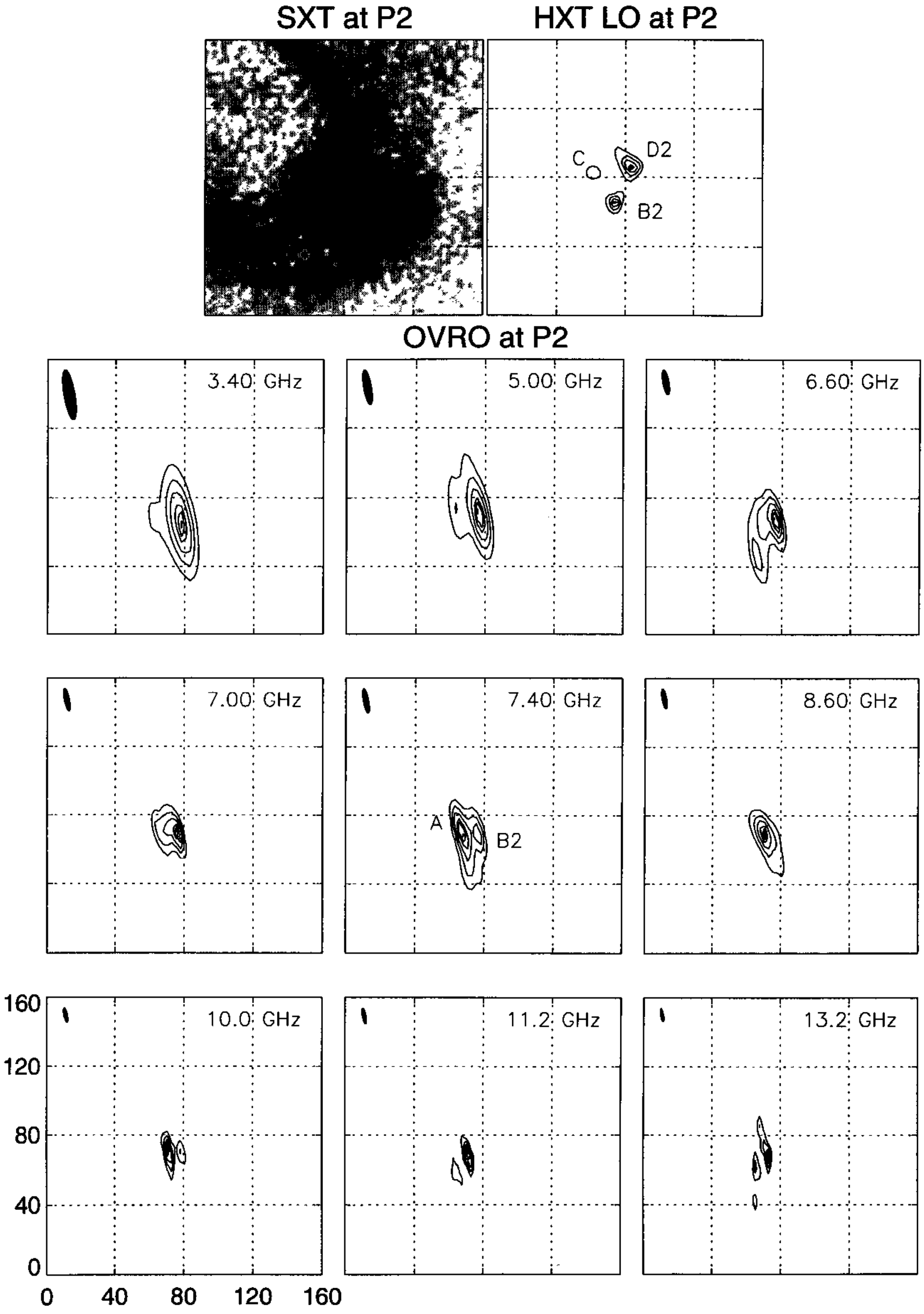

FIG. 15.—OVRO maps at different frequencies from 3.4 to 13.2 GHz made at P2. The contour levels are 20%, 40%, 60%, 80%, 90%, and 100% of the peak flux density at each frequency. Note that between 7.0 and 7.4 GHz the main source changes from being source B2 to source A. The two top panels are SXT and HXT LO maps at P2.

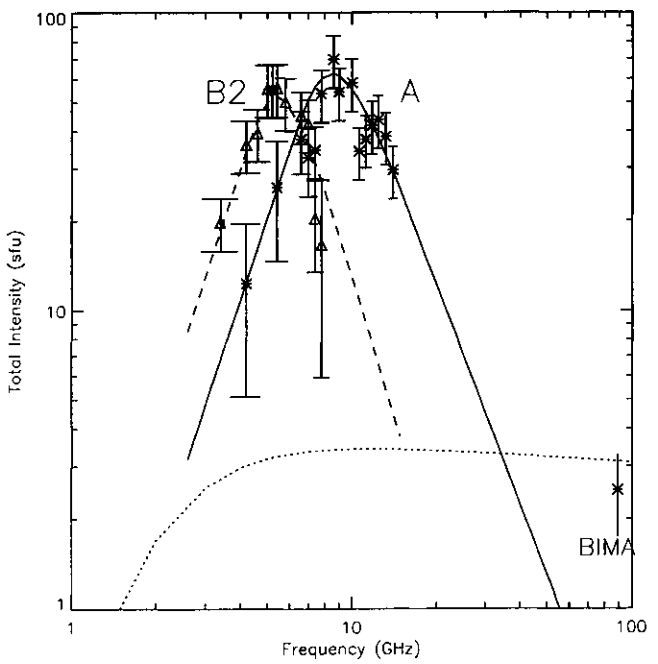

FIG. 16.—OVRO spectra of sources A and B2 at P2, with the millimeter point at 86 GHz. The solid and dashed lines are models of gyrosynchrotron emission from sources A and B2, respectively (§ 8.2). The dotted line represents the free-free spectrum from the soft X-ray–emitting source A, at P2.

results are discussed in detail in § 8.2.

The last phase, PM, appears to be purely thermal, with gradual soft X-ray emission from loop AB dominating. Microwave (>3 GHz) and hard X-ray emissions have ceased, and no further electron acceleration is observed. The millimeter radiation peaks at this time (PM), suggesting a thermal origin for its emission. Since it is not possible to determine the location of the millimeter source, we are unable to associate the millimeter emission with the sources observed at other wavelengths.

8.1. *Energetics of the Flare*

8.1.1. *Nonthermal Energy*

The rate of energy input from the accelerated electrons, P_e, can be estimated from power-law hard X-ray spectra (Hudson, Canfield, & Kane 1978). If the hard X-rays are produced by nonthermal electrons in the thick-target model (which assumes that the electrons are stopped in the source, as should be the case for footpoint emission), then

$$P_e = 1.33 \times 10^{25} \frac{a\gamma}{\beta(\gamma - 1, 1/2)} E_0^{1-\gamma} \text{ ergs s}^{-1} , \quad (2)$$

where γ is the spectral slope of the photon spectrum, a is the extrapolated photon flux at 1 keV (see eq. [1]), E_0 is the electron low-energy cutoff, and β is the standard beta function. On the other hand, if the hard X-rays are produced at a loop top, where the ambient density is low, then the expression for the thin-target case (which assumes that the electron spectrum is not significantly changed during the emission of the X-rays) should be used:

$$P_e = 4.09 \times 10^{23} \frac{a\gamma}{n_i L_9(\gamma - 3)\beta(\gamma - 1, 1/2)} E_0^{3-\gamma} \text{ ergs s}^{-1} , \quad (3)$$

where L_9 is the loop height along the line of sight in units of 10^9 cm and n_i is the ion density (cm^{-3}) in the emitting region. The power injected by the nonthermal electrons is calculated for the individual sources B1, B2, C, D1, D2, and G in HXT maps. All sources are assumed to be thick-target except for loop-top source B2, for which we use the thin-target calculation. The total energy deposition, ϵ_{inj}, by the energetic electrons is obtained by integrating P_e over time, which is a function of the cutoff energy E_0.

8.1.2. *Thermal Energy*

The energy contained in the hot thermal plasma, ϵ_{th}, at a given instant of time t can be determined by using the spatially resolved temperature and emission measure from the SXT images and is given by

$$\epsilon_{\text{th}} = 3n_i V k_B T = 3\sqrt{V}\sqrt{\text{EM}(t)}k_B T(t) , \quad (4)$$

where $n_e = n_i = n/2$ for a neutral plasma, k_B is the Boltzmann constant, and V is the volume of the hot plasma. The volume is assumed to be $V = A^{3/2}$, where A is the area of the source estimated from SXT images. In order to estimate how much energy is present in the flare plasma, we have subtracted the preflare thermal energy from ϵ_{th} for all times. Table 3 contains the maximum thermal energy ϵ_{th} (preflare-subtracted), the total injected energy $\epsilon_{\text{inj}}(E_0)$ for each source calculated by using the spectral index γ obtained from the HXT maps (described below), and the injected energy ϵ_{20} for a fixed $E_0 = 20$ keV.

The hard X-rays are produced by bremsstrahlung from energetic nonthermal electrons as they lose their energy in the lower corona and chromosphere. If the energy deposited by these electrons goes into heating the plasma to high enough temperatures, so that it will emit soft X-rays through thermal bremsstrahlung and atomic line emission, then the integral of the injected electron energy should match the thermal-energy time profile of the heated plasma if losses can be neglected, i.e.,

$$\epsilon_{\text{inj}}(t) = \int P_e(t)dt = \epsilon_{\text{th}} . \quad (5)$$

This is the so-called Neupert effect (Neupert 1968; Hudson 1991). We investigate whether the Neupert effect is taking place in the various soft X-ray sources in this flare. The injected and thermal energies are calculated by using the physical parameters estimated within the boxes shown in Figure 7 (repeated in the upper left panel of Fig. 17). We choose the low-energy cutoff, E_0, such that the injected energy, ϵ_{inj}, matches the rise of the instantaneous thermal energy output, ϵ_{th}, for each source (Fig. 17). Since source A has no hard X-ray counterpart, only its thermal energy is plotted. Because source B2 is thought to be located at a loop top, P_e was calculated by assuming a thin target (eq. [3]) whereas the power input, P_e, for all other sources was assumed to follow equation (2) for a thick target.

The thermal and nonthermal energy profiles agree well for sources B1 and B2 for $E_0 \sim 15$ keV, which suggests that the Neupert effect is applicable for these sources. The energy profiles do not agree for the impulsive sources C, D1, D2, and G. Even though the rise phase of the thermal and nonthermal energies agrees for sources D1 and D2, the model implies that more energy was injected than was radiated. Even when soft X-ray emission from the entire BD loop is considered, there is still an excess of injected energy. Note that the thermal energy of source G is much smaller

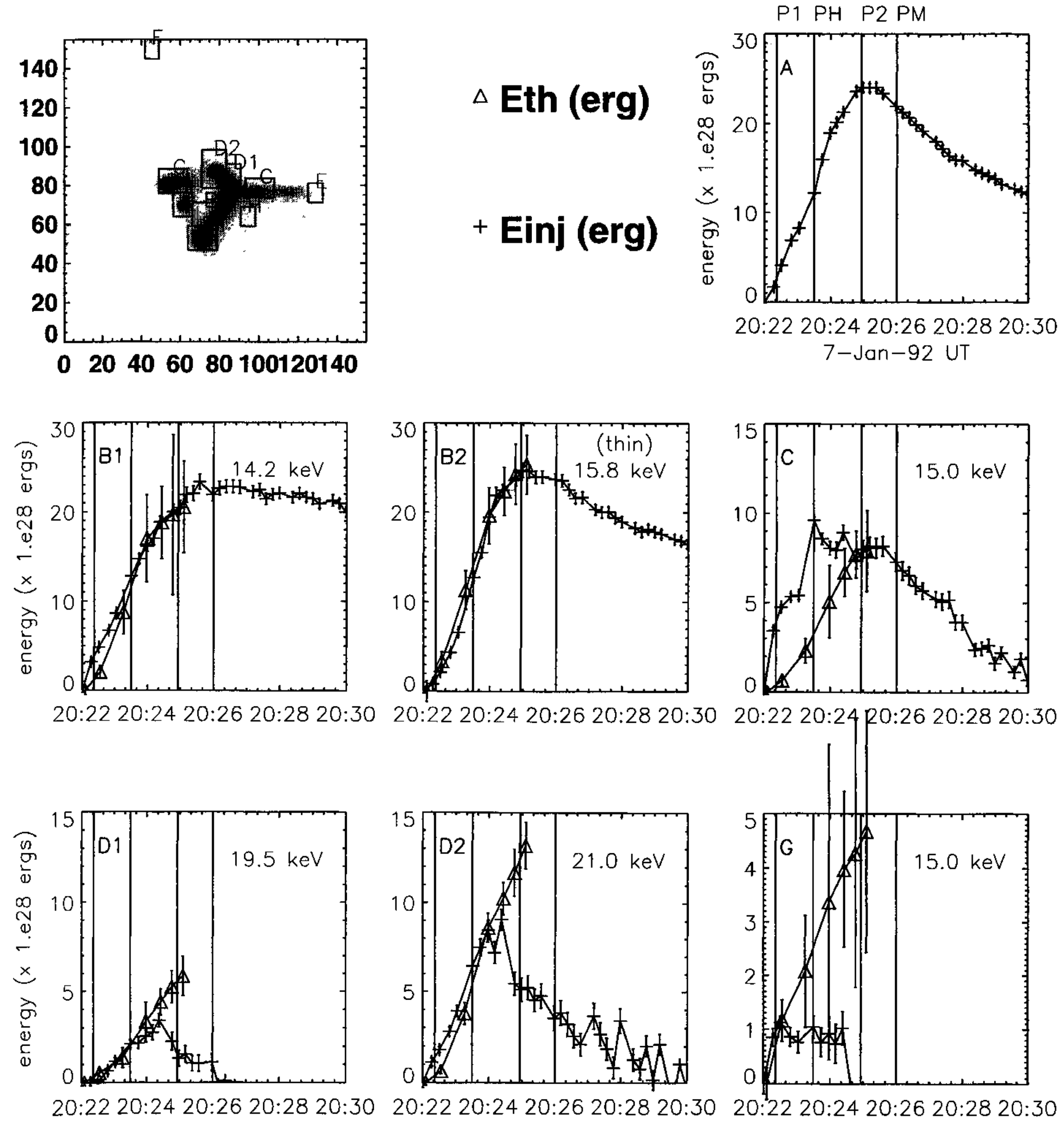

FIG. 17.—Thermal and injected energy (assuming thick-target model for all sources except source B2, for which thin target is assumed) for sources B1, B2, C, D1, D2, and G as a function of time. The top left panel shows the boxes used in determining the sources' physical parameters. Since there were no hard X-rays measured for source A, only its thermal energy is plotted, at the upper right. The cutoff energy, E_0, was determined for each source such that the rise slope of ϵ_{inj} matched that of ϵ_{th}.

(5%) than that of the stronger sources. The total injected energy from all sources (including those not listed in Table 3) adds up to 8×10^{29} ergs. However, for a fixed cutoff energy of 20 keV, the total energy in energetic electrons for the entire flare is $\sim 4.3 \times 10^{29}$ ergs.

The photospheric magnetic field at sites C, D1, D2, and G is weaker than that of the other sources. This weak magnetic field allows the electrons to penetrate deeper into the chromosphere, and thus much of the electron energy may have gone into heating the chromosphere below, hence no significant soft X-ray emission was produced.

8.2. *Hard X-Ray and Microwave Emission*

Many authors (e.g., Kundu 1961; Kai 1987) have suggested a common origin for the hard X-ray and microwave emission based on the observed similarity of the time profiles. A similar time profile is expected if most of the accelerated electrons precipitate down to the chromosphere by spiraling along the magnetic field, giving rise to radio emission in the lower corona and hard X-rays in the chromosphere (Kai 1986). It must be pointed out that the electrons producing the microwave emission are expected to have energies usually of the order of a few hundred keV whereas the hard X-rays measured by HXT originate from electrons of tens of keV energy. Thus a substantial extrapolation in energy is required; some observations indicate that the spectrum does not remain a single power law over that range of energies (Lin & Schwartz 1987; Dennis 1988; Dulk, Kiplinger, & Winglee 1992; Kundu et al. 1994; Silva et al. 1996a). A direct comparison of the emission at both wavelengths would thus require measurements of the hard X-rays up to several hundred keV.

The energy distribution of the nonthermal electrons that produce the hard X-ray emission is assumed to follow a power law, given by equation (B1) (see Appendix B). Table 3 contains the inferred electron spectral index, δ, and energetic electron density, $n_e(E > E_0)$, from the power-law fits to the hard X-ray photon spectrum at P2 for the hard X-ray sources B1, B2, C, D1, D2, and G. The energetic electron density was calculated by assuming a volume, $V = A^{2/3}$, where A is the area of the individual boxes shown in Figure 17. The total number of nonthermal accelerated electrons above E_0 for each individual source was calculated by using equation (B2) in Appendix B, for both thin- and thick-target cases.

A thin target may be assumed for emitting electrons located at the top of the magnetic loop (see, e.g., Kane & Anderson 1970). If the energy distribution of the loop-top electrons remains basically unchanged, then the accelerated electron distribution is assumed to be the same as the instantaneous distribution. In this case, the energetic electron density $n_e(E > E_0)$ is calculated by using $\delta_{\rm inst}$ and $K_{\rm inst}$ given by equation (B4). The $n_e(E > E_0)$ and $\delta_X = \delta_{\rm inst}$ are listed in the first row for each source of Table 3 (labeled "inst" in the electron population column). Conversely, in the "thick-target" model (Hudson 1972), the electrons precipitate down into the chromosphere, a much denser region, where they lose all their energy through Coulomb collisions. The accelerated electron spectrum can be related to the instantaneous electron spectrum by a continuity equation (Lin 1974). In this case, $\delta_X = \delta_{\rm acc}$ and $n_e(E > E_0)$ are determined by using $\delta_{\rm acc}$ and $K_{\rm acc}$ from equation (B6). The electron density, $n_e(E > E_0)$, and the power-law index, δ_X, are listed in the second row of Table 3 for each source (labeled "accel"). The area of the hard X-ray source, $\Delta\Omega$, used in the computation of the parameters listed in Table 3, measured from HXT maps, is ~ 120 arcsec^2 (equivalent to a circular source of 6″ radius) for all three sources at P2. This value of $\Delta\Omega$ is used in equations (B4) and (B6).

8.2.1. *Gyrosynchrotron Emission*

Source B2 is common to both OVRO and HXT maps during P2. The hard X-ray sources C and D2 are not seen in the microwave maps, probably as a result of the fact that they overlie regions of low photospheric magnetic fields. The photospheric magnetic field strengths, as measured in the MSFC magnetogram (Fig. 2, *top*), are ~ 140 and ~ 270 G at sites C and D2, respectively. Conversely, source A, which overlies a region of stronger magnetic field (~ 600 G), was only detected in the microwave maps. Since the photospheric magnetic field at A is stronger than at sites C or D2, magnetic mirroring at footpoint A may explain why source A is not seen at hard X-ray wavelengths.

The shape of the spectrum of the OVRO sources A and B2 (Fig. 16) at P2 suggests that the microwave emission is due to gyrosynchrotron radiation from nonthermal electrons. In the optically thin regime ($\tau_\nu \ll 1$), the gyrosynchrotron flux density can be approximated by $S_\nu \propto \nu^{-\alpha}$. The electron power-law index, δ, can be determined from the high-frequency, optically thin, slope of the spectrum, α (see Dulk 1985, eq. [35]):

$$\alpha = 0.90\delta - 1.22 . \tag{6}$$

A relation between α (the microwave optically thin spectral slope) and γ (the hard X-ray photon flux spectral index) can be obtained by assuming that the few-hundred-keV electrons responsible for the radio emission have the same power-law index δ as the $\lesssim 100$ keV electrons producing the hard X-ray radiation. For the thin-target model, equation (6) results in $\alpha = 0.90\gamma - 1.67$, whereas, in the thick-target case, $\alpha = 0.90\gamma + 0.13$ (see Appendix B for relations between δ and γ for both cases).

By fitting the observed spectra with gyrosynchrotron radiation (Dulk 1985, eqs. [35] and [36]), the following parameters may be constrained: the electron density (n_e), spectral index of the electron energy distribution (δ), magnetic field strength (B), and microwave source radius (r). The angle θ between the magnetic field line and the line of sight is assumed to be $\theta = 50°$ for source A, a footpoint source, and 80° for the loop-top source B2. As discussed in § 7.3, the microwave sources' sizes are further constrained by the fact that they were unresolved by the interferometer. The radius of source A is $r \leq 3''$, and for source B2, $r \leq 5''$. The magnetic field strength at the microwave source site is also constrained by the measured photospheric fields, which are maximum values. Thus $B < 600$ G for source A, and $B \ll 650$ G for the loop-top source B2.

Unfortunately, the high-frequency slope of OVRO sources is highly uncertain, as can be seen in Figure 16. Nevertheless, model fits to the microwave spectrum of sources A and B2 were obtained and are plotted as solid (source A) and dashed (source B2) lines in Figure 16. The fit to the microwave spectrum of source A yields $\delta_r = 4.1$, $n_e(E > 10 \text{ keV}) = 10^8$ cm^{-3}, $r = 3''.0$, and $B = 500$ G while the parameters for source B2 are $\delta_r = 4.9$, $n_e(E > 10$ keV$) = 10^8$ cm^{-3}, $r = 6''.0$, and $B = 370$ G. We point out that steeper values of δ_r would require higher values of n_e, B, and r, which are already close to their upper limits. The size of source B2 obtained from the spectral fit, slightly above the beam size, is still within the uncertainties of source size measurements from OVRO maps. The parameters that resulted from the fit are listed in Table 3.

A comparison of the power-law slope of the differential electron energy spectrum for source B2 inferred from the radio spectrum with that derived from the hard X-ray maps suggests that the electron energy distribution is not a single power law. As mentioned earlier, the hard X-rays observed here originate from electrons with less than 100 keV in energy whereas the microwave emission is believed to be generated by electrons of a few hundred keV. Thus the differential energy spectrum of the accelerated electrons from B2 is more likely a double power law, with $\delta = \delta_X = 4.2$ below ~ 100 keV, whereas $\delta = \delta_r = 4.9$ above this break energy. The gyrosynchrotron flux density from source A at 86 GHz is well below that measured by BIMA. However, because of its gradual time profile, we do not believe the millimeter emission to be nonthermal. The millimeter emission is discussed in detail in the following section.

8.3. *Millimeter Emission*

There are two possible mechanisms that can generate millimeter-wave emission (Kundu et al. 1990): nonthermal gyrosynchrotron and thermal bremsstrahlung. Thermal gyrosynchrotron has been ruled out because of its very steep slope ($\propto \nu^{-8}$), which implies a millimeter flux density much smaller than that observed from flares at these wavelengths (White & Kundu 1992). It is worth pointing out that thermal millimeter emission is sensitive to plasmas over a wide range of temperatures, as opposed to soft X-rays, which are sensitive to million-kelvin temperatures (Kundu et al. 1990). By combining the 86 GHz flux density with the microwave flux densities obtained from the single-frequency maps (§ 7.3), the type of mechanism that created the millimeter emission may be identified.

8.3.1. *Gyrosynchrotron Emission*

Can the millimeter emission be associated with source A or B2, seen by *Yohkoh* and OVRO? There may be other sources within the OVRO maps, but because of the poor (u, v)-coverage of the single-frequency maps (dynamic range of 10:1), a secondary source with an intensity $\lesssim 20\%$ of the main source cannot unambiguously be identified. Thus, if there was a source present in the BIMA field of view, its flux density was less than 5–10 sfu at 10 GHz. The VLA observed a 1.5 GHz source, J, within BIMA's field of view. This was the strongest 1.5 GHz source at P2. This source, however, was not detected at higher frequencies in the OVRO data, which indicates that it had a very steep spectrum and would not have been detected at 86 GHz.

As shown in Figure 16, the millimeter emission detected by BIMA, even within its 30% error bar, is well above that expected from gyrosynchrotron emission from source A. Moreover, the temporal evolution of the millimeter emission is very different from the microwave and hard X-ray time profiles, suggesting that the millimeter radiation was not created by the same mechanism that produced the microwave and hard X-ray emissions.

8.3.2. *Free-Free Emission*

The millimeter emission could also be thermal bremsstrahlung (Silva et al. 1996b). The radio flux density produced by the free-free emission of a hot plasma can be calculated by using the soft X-ray temperature and emission measure (White & Kundu 1992; note that their expression, eq. [6], is for one polarization only and must be multiplied by 2 in order to obtain the total intensity). At high microwave frequencies and above, this emission is optically thin, and the free-free emission is independent of frequency (for a constant source size):

$$S_{\rm free} \simeq 27.3 \frac{\rm EM_{49}}{\sqrt{T_{\rm MK}}}\ {\rm sfu} \quad (\tau \ll 1)\,, \tag{7}$$

where $\rm EM_{49}$ is the emission measure in units of 10^{49} cm^{-3}, and $T_{\rm MK}$ is the temperature in millions of kelvins. $S_{\rm free}$ can be determined by using the temperature and EM obtained from SXT maps rather than the *GOES* data, which are an average over the entire emitting region.

The dotted line in Figure 16 represents the free-free emission from the soft X-ray source A at P2. The calculation of the free-free emission was performed by using the temperature and emission measure listed in Table 3 and a source diameter of 30″. As seen in the thermal radio spectra of source A at P2, the free-free flux density from source A at 86 GHz agrees with the BIMA observations within its uncertainties. Figure 18 shows the temporal behavior of the inferred free-free radio flux density at 86 GHz from source A and that of BIMA's shortest baseline, corrected for the 110″ pointing offset of the telescope. The radio flux density from source A peaks at PM, like the observed BIMA radiation, and measures ~4.2 sfu. The uncertainty in BIMA's amplitude calibration is ~30% and agrees well with the radio flux density inferred from the hot plasma at A. However, the predicted radio intensity remains higher longer than the observed millimeter-wavelength emission. This may imply that the source is expanding in size. The *Yohkoh* SXT images (Fig. 6) suggest the source to increase from 8″ (in the east-west direction) at PM to 16″ some 3 minutes later. Recalling that the shortest baseline had a fringe spacing of 25″, sources over 8″ in size would be resolved out, causing the total observed flux density to decrease. The vertical bars plotted in Figure 18 indicate the decrease in flux density of the free-free radio flux density if the source expands as seen in the *Yohkoh* SXT images. The vertical extent of the bars reflects the errors in the size estimates.

Since the millimeter emission is also sensitive to cooler material lower in the atmosphere, there is a possibility that the 86 GHz emission is coming from a lower temperature plasma at the position where the telescope was pointing, which is not visible in soft X-rays. However, the existence of such a cool source would increase the free-free flux density

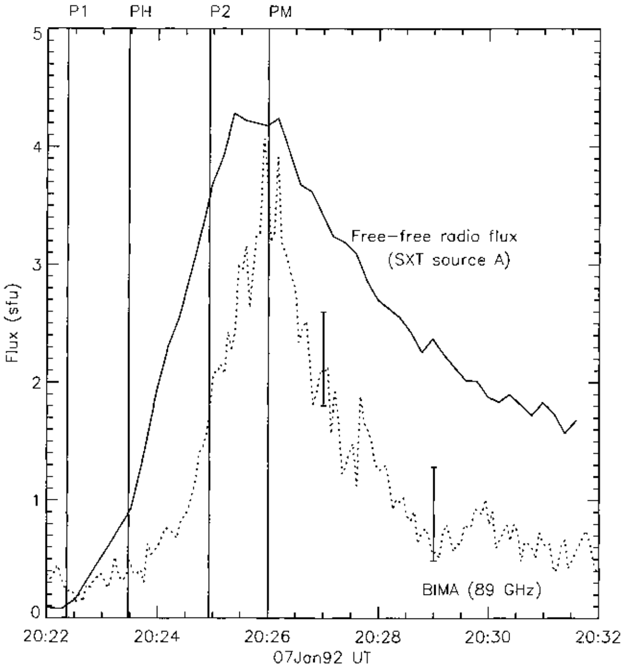

FIG. 18.—Calculated optically thin free-free radio flux density at 86 GHz (eq. [7]) from the SXT source A (*solid line*) and the millimeter (86 GHz) flux density as measured by BIMA's shortest baseline (*dashed line*), corrected for the 110″ pointing offset. The vertical bars indicate how the flux density measured by BIMA would decrease as the source expands (linear size measured from SXT high-resolution images) and is partially "resolved out" by the interferometer.

at millimeter wavelengths ($S_{\rm free} \propto T^{-1/2}$; see eq. [7]), hence increasing the discrepancy between the observed and inferred radio flux density.

9. CONCLUSIONS

The Hα, X-ray, and microwave images reveal a remarkable complexity in the C8.9 flare on 1992 January 7. The main soft X-ray loop (AB) is located over a delta sunspot, which has a strongly sheared magnetic field along its neutral line. There is also evidence of emergence of new magnetic flux polarity at this spot. The flare consisted of three bursts of particle acceleration (P1, PH, and P2) followed by a purely thermal phase (PM). At the time of the first acceleration phase, P1, several different sites (A, B1, C, D1, D2, E, F, and G) brighten simultaneously and are probably all connected to the energy-release site located above the loop tops. Since the coronal source H is seen to brighten before P1 in VLA 5.0 GHz maps (its time profile is shown in Fig. 12), and because it is connected to the brightest 23–33 keV source (G) seen in the HXT M1 map at P1, we believe that the first energy release occurred near source H, at the top of loop BG. Source H, barely seen in the hard X-ray maps at P1, may be similar to the hard X-ray sources seen above the top of soft X-ray loop observed by Masuda et al. (1994). Those authors suggest that these sources are located just below the site of magnetic reconnection where the flare energy is first released. The fact that the 1992 January 7 flare was a much smaller flare, in which far fewer high-energy electrons were accelerated, may explain why source H was so weak in *Yohkoh* HXT maps at P1.

During P1, most of the energetic electrons travel from the energy release site, above source H, to G (the brightest source in HXT M1 maps). Source G is probably a footpoint of a loop that connects to source B1 (loop BG), with source H at its apex. Since no significant thermal emission is detected from source C, D1, D2, or G, we conclude that the energy was deposited low in the chromosphere because the resultant heating did not produce much plasma at soft X-ray–emitting temperatures. According to the photospheric magnetograms, the magnetic field at C, D1, D2, and G is weaker than at the other footpoint, B1. This facilitates the precipitation of accelerated electrons deep into the chromosphere since there would be less mirroring. No microwave emission from gyrosynchrotron processes is expected to be detected at C, D1, D2, or G, because of the weaker magnetic field, and indeed no microwave source was observed.

The second phase, PH, is characterized by softer spectrum acceleration. Source B2 is the dominant feature in the HXT LO map, and no significant X-ray (>23 keV) or microwave emission is detected at this time. Thus the site of electron acceleration may have changed from the top of loop BG to the top of loop AB. Alternatively, this period could be interpreted as a thermal phase due to the steep hard X-ray spectral slope of source B2. However, the excellent agreement of computed cumulative injected electron energy with thermal plasma energy, i.e., the Neupert effect, and the observed blueshifts in soft X-ray lines detected by BCS shortly after PH favor the nonthermal interpretation.

Microwave maps at P2 show the two sources associated with loop AB (A, not seen by HXT, and B2). From gyrosynchrotron fits to the spectra, magnetic fields of 370 G for source B2 (loop apex) and 500 G for source A (footpoint) were estimated. By comparing the radio and hard X-ray observations, the differential energy spectrum of the electrons from source B2 was found to be a double power law that breaks down at $\sim$100 keV.

The last phase, PM, is characterized by maxima in the gradual soft X-ray and millimeter emissions. The hard X-ray and microwave emissions have ceased by this time, and no further particle acceleration is detected, indicating that PM is purely thermal. Assuming that the BIMA emission originated from source A, the millimeter emission is consistent with thermal bremsstrahlung from the soft X-ray–emitting hot plasma.

Only the gradual X-ray sources B1 and B2 display the Neupert effect: the total injected energy from the accelerated electrons equals the maximum instantaneous thermal energy of (2–2.5) $\times 10^{29}$ ergs for each of these sources. The sum of the injected electron energy of the individual sources, as estimated from the hard X-ray spectra, is $\sim 10^{30}$ ergs. We can compare the total injected energy with the magnetic energy at the energy release site B2. The magnetic energy available for the flare, $E_B = B^2 V/(8\pi)$, can be estimated from the magnitude of the magnetic field inferred from the microwave observations. The magnetic field at the top of loop AB is $\sim$370 G, which implies $E_B = 2 \times 10^{31}$ ergs for an area $A = 2.5 \times 10^{18}$ cm^2 ($V = A^{3/2}$). Note that only a fraction of this energy is free energy. Thus the total flare energy is still an order of magnitude less than the magnetic energy contained in the loop top.

Some puzzles remain: (1) There are a number of sources outside the two main magnetic loops. For most sources the connecting soft X-ray loop is not observed, e.g., sources G and H and the VLA low-frequency (1.5 GHz) radio source J. For source F, a soft X-ray loop is seen; however, the connection to the main flaring region (C, D1, or D2) is not clear. (2) Because of the lack of spatial resolution, it is not possible to determine where the millimeter emission originates. BIMA is being upgraded to nine antennas, which will make it possible to image millimeter emission for future solar flares. These types of observations are necessary to determine the millimeter-emission mechanisms.

We conclude that a multiwavelength analysis is crucial to forming a global picture of a solar flare and to understanding the physical processes involved in the energy release, particle acceleration, and the plasma response.

A. V. R. S. would like to thank J. Lim for fruitful discussions. We thank Alan Kiplinger and Dave Speich for their coordination during the Max '91 campaign and NSF and NASA for their support of the Max '91 campaign. We also thank the *Yohkoh* team. We are grateful to Greg Deuel for providing the RSTN data. A. V. R. S. acknowledges partial funding from CNPq (Brazil), NSF grant AST 93-20238, Cal Space grant 14-92, and NASA grant NAGW-3005, which made possible a visit to Caltech in order to reduce OVRO data. The *Yohkoh* X-ray telescope was prepared by the Lockheed Palo Alto Research Laboratory, the National Astronomical Observatory of Japan, and the University of Tokyo with the support of NASA and ISAS. *Yohkoh* data analysis at the University of California, Berkeley, is supported by NASA under Lockheed subcontract SE80D7860R. Solar radiophysics at the University of Maryland is supported by NSF grant ATM 93-16972, NASA grant NAGW-1541, and NASA/CGRO grant NAG 5-1450. The use of BIMA for scientific research is supported by NSF grant AST 93-14847. H. S. H. acknowledges NASA contract NAS 8-37334 for support. J. G. D. would like to thank the Royal Society for a travel grant, which enabled a visit to Japan. M. J. H. acknowledges support by the Solar Physics Office of the Space Physics Division at NASA Headquarters.

APPENDIX A

INSTRUMENTS

A1. MARSHALL SPACE FLIGHT CENTER (Hα)

The Hα images from MSFC (Fig. 5) were acquired with a 16.5 cm aperture telescope through a Fabry-Perot filter with a 0.7 Å bandwidth. The images are obtained with a small CCD camera.

A2. *YOHKOH* SOFT X-RAY TELESCOPE

The SXT instrument is a glancing-incidence telescope that forms X-ray images in the 0.25–4.0 keV range on a CCD detector. When *Yohkoh* detects a flare, it goes into "flare mode" (see Tsuneta et al. 1991 for a detailed description), in which a rapid sequence of 64 × 64 pixel images at full (2''.455) resolution are taken by SXT through several filters.

A3. *YOHKOH* HARD X-RAY TELESCOPE

The *Yohkoh* HXT is a Fourier-synthesis–type imager consisting of 64 modulation subcollimators (Kosugi et al. 1991). Each subcollimator has a different pitch and/or position angle of collimator grids. The hard X-ray photons passing through a single subcollimator are periodically modulated with respect to the incident angle, which yields a modulation pattern of the corresponding subcollimator. The count rates obtained by each pair of detectors provide the amplitude and phase of a single spatial Fourier component of the hard X-ray image.

When a flare mode is triggered, the 64 hard X-ray count rates are accumulated with 0.5 s temporal resolution in four energy bands between 14 and 93 keV (LO, M1, M2, and H bands). The hard X-ray images are synthesized by use of the maximum entropy method.

A4. *YOHKOH* BRAGG CRYSTAL SPECTROMETER

The BCS consists of two bent-crystal spectrometers that observe the Fe XXV, Ca XIX, and S XV line complexes. Each spectrometer consists of a double detector placed behind a pair of germanium crystals that diffract the incoming X-rays into the detectors (Culhane et al. 1991).

The individual spectral lines in S XV, Ca XIX, and Fe XXV were fitted by using Voigt functions with damping parameters determined by the crystal rocking curve widths. Although the original BCS data for this event had an integration time of 3 s, the data had to be binned into 24 s intervals in order to obtain a reasonable count rate in the early rise phase. A two-component fit was used for the data taken before 2032:43 UT, where one component represents the assumed "stationary" plasma and the other represents the "moving" plasma. Fitting was done by using the method outlined by Fludra et al. (1989), i.e., the theoretical spectra were generated by using atomic data from Bely-Dubau et al. (1982a, 1982b).

Because of the presence of another active region within the field of view, the S XV spectra before PH could not be fitted. A data gap occurred from 2027:22 until 2032:43 UT while the spacecraft was in the South Atlantic Anomaly. Usable S XV and Ca XIX data are available until 2044:25 UT. Data taken after 2032:43 UT could not be fitted accurately with a two-component fit.

A5. VERY LARGE ARRAY

The VLA microwave interferometer consists of 27 identical 25 m reflector antennas arranged along three radial arms, forming a Y-shaped array (Thompson et al. 1980). The antennas can be moved on railroad tracks along the arms. Four standard configurations of antennas along the array arms are available. The VLA was in the B configuration during the campaign, in which the antennas are spread out over 6 km along each arm. This array configuration offers angular resolution of a few arcseconds, but is not sensitive to large structures, e.g., sources over 1' and 18'' in size cannot be seen at 1.5 and 5 GHz, respectively. Our observing modes consisted of alternating scans at 0.33 and 1.5 GHz (4 minutes long; both frequencies can be observed simultaneously), 5 GHz (4 minute scans), and 8.3 GHz (8 minute scans).

A6. OWENS VALLEY RADIO OBSERVATORY ARRAY

OVRO consists of five antennas distributed in an inverted-T configuration. Two of the dishes are large, 27 m in diameter, and the other three antennas are 2 m in size. The two large dishes are located on the east-west arm, together with one of the smaller dishes. The other 2 m antennas are located on the north arm (Lim et al. 1994). The spatial resolution of the array at the time of the flare was $217''/\nu_{\rm GHz}$ along the major axis of the CLEAN beam and $53''/\nu_{\rm GHz}$ along its minor axis (e.g., at 10 GHz, the spatial resolution was $22'' \times 5''$ along the major and minor axes, respectively). The baseline data were calibrated with respect to 3C 84.

By synthesizing close frequencies, the (u, v)-coverage in the data can be improved over that in single-frequency maps, which facilitates detection of the various sources in the maps. Once the position of the sources is known, single-frequency maps are made to determine the spectra of the individual sources.

Because of the need for sensitivity, only baselines including at least one of the 27 m antennas can be used for flares as weak as the one described in this paper. There were several problems with the large dish located at the west end of the east-west arm. Its pointing was offset $\sim 2'$ from the other dishes, which caused the data from that dish to be strongly attenuated at high frequencies. At frequencies lower than 5.0 GHz, the primary beam is sufficiently large that the data were unaffected. At higher frequencies, the flux densities have been corrected for the pointing offsets. The RCP data of this dish were lost since the RH feed was not working properly. The baselines with this antenna are mainly the longer ones. Therefore these long baselines are not included in the RCP maps, which results in a low spatial resolution.

A7. BERKELEY-ILLINOIS-MARYLAND ARRAY

At the time of the observation on 1992 January 7, BIMA consisted of three antennas, each 6 m in diameter, aligned in the east-west direction. The array was operating at 86 GHz with a temporal resolution of 0.4 s and sensitivity of $\sim$0.01–0.02 sfu (Kundu et al. 1990). As the interferometer had only three east-west baselines, it was not possible to construct images. The fringe spacing of the three baselines were 9", 15", and 24". For a source to be unresolved by the instrument, its size must be of the order of or smaller than one-third of these fringe spacings (i.e., less than 8"). Since the flux density on the three baselines is about the same, the source is probably unresolved by the interferometer. This agrees with the fact that the microwave source diameter is smaller than 10" (OVRO data, § 7.3).

APPENDIX B

MICROWAVE AND HARD X-RAY EMISSION

The nonthermal electrons that produce the hard X-rays and microwaves are assumed to be isotropically distributed over pitch angle, with an energy distribution of the form

$$N_e(E) = KE^{-\delta} \text{ electrons keV}^{-1} , \tag{B1}$$

where K is a constant. The number of electrons per cubic centimeter with energy $E > E_0$, i.e., $n_e(E > E_0)$, can be obtained by integrating equation (B1):

$$n_e(E > E_0) = KE_0^{1-\delta}/(\delta - 1) . \tag{B2}$$

Because of the spatial coincidence or proximity of microwave and hard X-ray sources, it is assumed that the same electrons are responsible for the radio and X-ray radiation. The hard X-rays are commonly assumed to originate at the footpoints of magnetic loops. If the microwave emission also originates from the footpoints, then the instantaneous hard X-ray–producing electron population are the same electrons that produced the nonthermal microwave emission. The accelerated electron spectrum can then be obtained from the hard X-rays under the thick-target assumption, where the X-ray–producing electrons lose their energy predominantly through collisions. On the other hand, if the microwaves are produced at the loop top and if the acceleration of electrons occurs at the loop top, the instantaneous electron distribution is used for the radio-emitting electrons (thin-target case).

The spectrum of the instantaneous electron population, $N_e(E)$, can be obtained from the bremsstrahlung spectrum, $I(h\nu)$, produced by these electrons. The electron flux, and therefore the photon flux, are assumed to be isotropic. The relation for $I(h\nu)$ (Brown 1971; Lin 1974) is given by

$$I(h\nu) = \frac{n_i V}{4\pi d^2} \int N_e(E) v(E) \sigma_B(E, h\nu) dE , \tag{B3}$$

where n_i is the ion density, V is the plasma volume, $d = 1$ AU, $v(E)$ is the velocity of electrons at energy E, and σ_B is the bremsstrahlung cross section, which can be approximated by the Bethe-Heitler formula (Jackson 1962, p. 771). Assuming that the X-ray spectrum is a power law given by equation (1), equation (B3) can be inverted to obtain the instantaneous electron spectrum, equation (B1) (Brown 1971). Using Tandberg-Hanssen & Emslie's (1988) equations (5.31) and (5.32) and equation (1) above, the constant K and spectral index δ in equation (B1) become

$$\delta_{\text{inst}} = \gamma - 0.5 , \qquad K_{\text{inst}} = \sqrt{\frac{m_e}{2}} \frac{4\pi a}{\Delta\Omega n_i L \kappa_{\text{BH}} \bar{Z}^2} \frac{(\gamma - 1)}{\beta(\gamma - 1, 1/2)} , \tag{B4}$$

where $\Delta\Omega$ is the X-ray source's angular size, $\kappa_{\text{BH}} = 7.9 \times 10^{-25}$ cm^2 keV is the constant in the Bethe-Heitler cross section, $\bar{Z}^2$ is the mean atomic weight squared (1.178 for solar corona conditions), and β is the standard beta function.

The ion density, n_i, can be calculated from *Yohkoh* soft X-ray data, assuming $n_i = n_e$ and a filling factor of 1:

$$n_i = \sqrt{\text{EM}/V} , \tag{B5}$$

where the volume is $V = A^{3/2}$ and A is the source area.

The accelerated electron spectrum must be related to the instantaneous electron spectrum by a continuity equation (Lin 1974; Johns & Lin 1992; Lin & Johns 1993). In the thick-target case, electron escape is assumed to be negligible, and Coulomb collisions are assumed to dominate the energy losses. The accelerated electron spectrum, of the form given by equation (B1), has the following constants:

$$\delta_{\rm acc} = \gamma + 1.5\,, \qquad K_{\rm acc} = \sqrt{\frac{m_e}{2}}\,\frac{4\pi a C}{\Delta\Omega \kappa_{\rm BH} \bar{Z}^2}\,\frac{\gamma(\gamma - 1)}{\beta(\gamma - 1, 1/2)}\,, \tag{B6}$$

where $C = 2\pi e^4 \ln \Lambda$ and $\ln \Lambda$ varies between 20 and 30 for solar values.

REFERENCES

Aschwanden, M. J., Dennis, B. R., & Benz, A. O. 1991, in Max '91 Workshop No. 3: Max '91/*SMM* Solar Flares—Observations and Theory, ed. R. M. Winglee & A. L. Kiplinger, 234

Bastian, T. S., & Gary, D. E. 1992, Sol. Phys., 139, 357

Bely-Dubau, F., Dubau, J., Faucher, P., & Gabriel, A. H. 1982a, MNRAS, 198, 239

Bely-Dubau, F., et al. 1982b, MNRAS, 201, 1155

Brown, J. C. 1971, Sol. Phys., 18, 489

Crannell, C. J., Gary, D. E., Hurford, G. J., Starr, R., & Kucera, T. A. 1991, in Max '91 Workshop No. 3: Max '91/*SMM* Solar Flares—Observations and Theory, ed. R. M. Winglee & A. L. Kiplinger, 192

Culhane, J. L., et al. 1991, Sol. Phys., 136, 89

Dennis, B. R. 1988, Sol. Phys., 118, 49

Dulk, G. A. 1985, ARA&A, 23, 169

Dulk, G. A., Kiplinger, A. L., & Winglee, R. M. 1992, ApJ, 389, 756

Fludra, A., Lemen, J. R., Jakimiec, J., Bentley, R. D., & Sylwester, J. 1989, ApJ, 344, 991

Gary, D. E., & Hurford, G. J. 1990, ApJ, 361, 290

Holman, G. D., Kundu, M. R., & Kane, S. R. 1989, ApJ, 345, 1050

Hudson, H. S. 1972, Sol. Phys., 24, 414

———. 1991, BAAS, 23, 1064

Hudson, H. S., Canfield, R. C., & Kane, S. R. 1978, Sol. Phys., 60, 137

Jackson, J. D. 1962, Classical Electrodynamics (New York: Wiley)

Johns, C. M., & Lin, R. P. 1992, Sol. Phys., 137, 121

Kai, K. 1986, Sol. Phys., 104, 235

———. 1987, Sol. Phys., 113, 165

Kane, S. R., & Anderson, K. A. 1970, ApJ, 162, 1002

Kiplinger, A. L., Labow, G., & Orwig, L. E. 1991, in Max '91 Workshop No. 3: Max '91/*SMM* Solar Flares—Observations and Theory, ed. R. M. Winglee & A. L. Kiplinger, 210

Kosugi, T., et al. 1991, Sol. Phys., 136, 17

Kundu, M. R. 1961, J. Geophys. Res., 66, 4308

Kundu, M. R., White, S. M., Gopalswamy, N., Bieging, J. H., & Hurford, G. J. 1990, ApJ, 358, L69

Kundu, M. R., White, S. M., Gopalswamy, N., & Lim, J. 1994, ApJS, 90, 599

Kundu, M. R., White, S. M., & Schmahl, J. E. 1989, Sol. Phys., 121, 153

Kundu, M. R., White, S. M., & Welch, W. J. 1991, in Max '91 Workshop No. 3: Max '91/*SMM* Solar Flares—Observations and Theory, ed. R. M. Winglee & A. L. Kiplinger, 11

Lim, J. M., Gary, D. E., Hurford, G. J., & Lemen, J. R. 1994, ApJ, 430, 425

Lim, J. M., White, S. M., Kundu, M. R., & Gary, D. E. 1992, Sol. Phys., 140, 343

Lin, R. P. 1974, Space Sci. Rev., 16, 189

Lin, R. P., & Johns, C. M. 1993, ApJ, 417, L53

Lin, R. P., & Schwartz, R. A. 1987, ApJ, 312, 462

Masuda, S., Kosugi, T., Hara, H., & Ogawara, Y. 1994, Nature, 371, 495

McTiernan, J. M., Kane, S. R., Loran, J. M., Lemen, J. R., Acton, L. W., Hara, H., Tsuneta, S., & Kosugi, T. 1993, ApJ, 416, L91

Neidig, D. G., Kiplinger, A. L., Cohl, H. S., & Wiborg, P. H. 1993, ApJ, 406, 306

Neupert, W. M. 1968, ApJ, 153, L59

Nitta, N., Dennis, B. R., & Kiplinger, A. L. 1990, ApJ, 353, 313

Nitta, N., White, S. M., Schmahl, E. J., & Kundu, M. R. 1991, Sol. Phys., 132, 125

Schwartz, R. A., & Drake, S. A. 1991, in Max '91 Workshop No. 3: Max '91/*SMM* Solar Flares—Observations and Theory, ed. R. M. Winglee & A. L. Kiplinger, 57

Silva, A. V. R., Gary, D. E., White, S. M., Lin, R. P., & de Pater, I. 1996a, Sol. Phys., submitted

Silva, A. V. R., White, S. M., Lin, R. P., de Pater, I., Shibasaki, K., Hudson, H. S., & Kundu, M. R. 1996b, ApJ, 458, L49

Tandberg-Hanssen, E., & Emslie, A. G. 1988, The Physics of Solar Flares (Cambridge: Cambridge Univ. Press)

Thompson, A. R., Clark, B. G., Wade, C. M., & Napier, P. J. 1980, ApJS, 44, 151

Tsuneta, S., et al. 1991, Sol. Phys., 136, 37

Vaiana, G. S., Krieger, A. S., & Timothy, A. F. 1973, Sol. Phys., 32, 81

White, S. M., & Kundu, M. R. 1992, Sol. Phys., 141, 347

White, S. M., Kundu, M. R., Bastian, T. S., Gary, D. E., Hurford, G. J., Kucera, T., & Bieging, J. H. 1992, ApJ, 384, 656

Willson, R. F., Klein, K.-L., Kerdraon, A., Lang, K. R., & Trottet, G. 1990, ApJ, 357, 662